

A Modeling Study on the Development of a Bowing Structure and Associated Rear Inflow within a Squall Line over South China

ZHIYONG MENG

*Laboratory for Climate and Ocean–Atmosphere Studies, Department of Atmospheric and Oceanic Sciences,
School of Physics, Peking University, Beijing, China*

FUQING ZHANG AND PAUL MARKOWSKI

Department of Meteorology, The Pennsylvania State University, University Park, Pennsylvania

DUOCHANG WU

*Laboratory for Climate and Ocean–Atmosphere Studies, Department of Atmospheric and Oceanic Sciences,
School of Physics, Peking University, Beijing, China*

KUN ZHAO

School of Atmospheric Sciences, Nanjing University, Nanjing, China

(Manuscript received 2 May 2011, in final form 5 October 2011)

ABSTRACT

Through convection-permitting simulations, this study examines a large bowing structure within a squall line that occurred during the rainy season in South China. The bowing structure is closely associated with a local enhancement of (and balance between) the cold pool and the line-normal environmental low-level vertical shear. Rear inflow plays an essential role in the formation and evolution of this large bowing structure. It is found that the low-level rear inflow is largely a natural consequence of the baroclinically generated horizontal vorticity near the surface, while the midtropospheric rear inflow is forced by several pairs of bookend vortices. Vorticity budget and vortex-line analyses show that the bookend vortices form mainly through the tilting of horizontal vorticity. Consolidation of these pairs of bookend vortices forms a broad zone of contiguous rear inflow. The environmental flow and horizontal pressure gradient force associated with the midlevel pressure deficit induced by the rearward-tilting buoyant updrafts, on the other hand, are not primarily responsible for the formation of the rear inflow.

1. Introduction

Squall lines are among the most common modes of deep moist convection on earth. Radar images show that some squall lines assume an arc shape either partially or as a whole. The bowing structure of squall lines is usually associated with swaths of damaging winds (Fujita 1978).

There is a natural tendency for the updraft region in a squall line to tilt rearward (i.e., over the cold pool) in time as the convective system matures, owing to the increasingly

rearward-directed horizontal pressure gradient force experienced by air parcels ascending through the updraft region. Numerical simulations (e.g., Weisman 1992) have shown that the rearward-tilted updraft region results in a midlevel pressure deficit above the negatively buoyant cold pool and beneath the positively buoyant updraft (the rearward tilt allows the region of positive buoyancy to reside above the negatively buoyant cold pool). The midlevel pressure deficit results in a forward acceleration of air from the rear of the convective system, resulting in the so-called rear inflow that is typical of trailing-stratiform squall lines. The rear inflow has been regarded as a main contributor to the bowing structure of a squall line; its presence can be signified by an area of weak radar echo at the back edge of the stratiform region, likely due to evaporation and melting

Corresponding author address: Dr. Zhiyong Meng, Department of Atmospheric and Oceanic Sciences, School of Physics, Peking University, Beijing, China.
E-mail: zymeng@pku.edu.cn

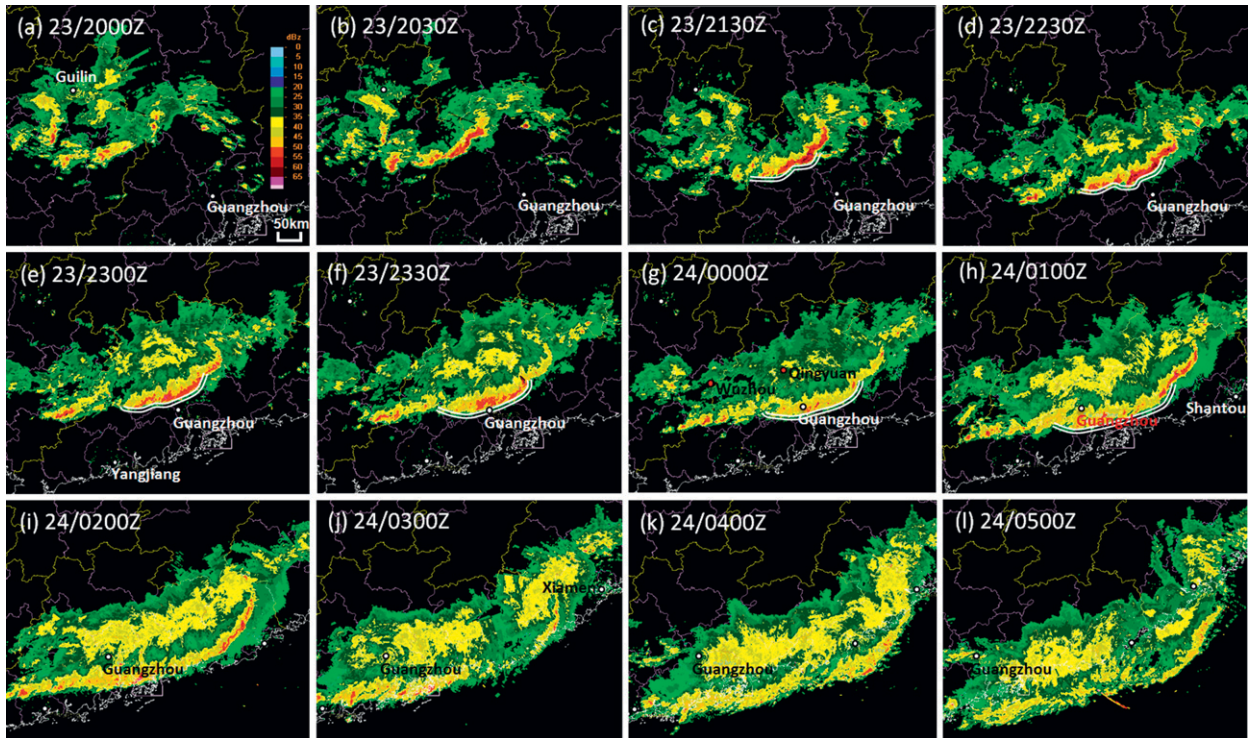


FIG. 1. Observed evolution of the squall line and its bow segments.

(Przybylinski and Gery 1983; Smull and Houze 1985, 1987). This weak-echo channel was termed “rear-inflow notch” (RIN) by Przybylinski (1995).

The rear inflow can be induced or enhanced by book-end vortices—a pair of midlevel counterrotating vortices that usually appear at each end of the bow-shaped line segment behind the leading edge of active convection, with a dimension of tens of kilometers at midlevels (3–7 km) (Weisman 1993; Atkins et al. 2004). Observational studies have shown that bow echoes in most squall lines first have symmetric line-end vortices but the cyclonic vortex will later become more intense than the anticyclonic vortex (Houze et al. 1989; Loehrer and Johnson 1995; Scott and Rutledge 1995; Wheatley and Trapp 2008). Weisman (1993) proposed that bookend vortices may initially form through downward tilting of horizontal vorticity associated with the environmental vertical shear. Weisman and Davis (1998) further examined the sources of the horizontal vorticity in cases with different low-level vertical shear and demonstrated that the bookend vortices are likely to be maintained through upward tilting of baroclinically generated horizontal vorticity within the convection, and that the conceptual model proposed by Weisman (1993) may only explain part of the strong-shear cases at the initial stage. The midlevel environmental wind is also reported to be capable of overtaking a squall line from behind that

contributes to the system’s rear inflow (Zhang and Gao 1989).

Using airborne Doppler radar observations, Grim et al. (2009) examined the relative importance of different contributing factors on the formation and evolution of rear inflow for a rapidly developing and decaying squall line. They found that the pressure gradient associated with the irrotational wind component, horizontal vorticity, and bookend vortices were the dominant forcing mechanisms at the initial stage. At later times, the main forcing mechanism shifted to a combination of a midlevel mesocyclone due to the vertical buoyancy gradient and the bookend vortices. The impact from ambient flow was shown to have played a minor role in that case.

The above hypotheses are mostly based on observations or idealized numerical simulations with squall lines that are maintained by lifting over their own evaporatively driven cold pools as summarized by Fritsch and Forbes (2001). These features may change because of spatial and temporal heterogeneity in the background environment in more realistic scenarios (Stensrud and Fritsch 1991; Jewett and Wilhelmson 2006). Whether these hypotheses apply to bowing structure of squall lines that are maintained by lifting over a frontal surface in an actual environment with cloud-resolving numerical simulations is an open question. The current study performs convection-permitting

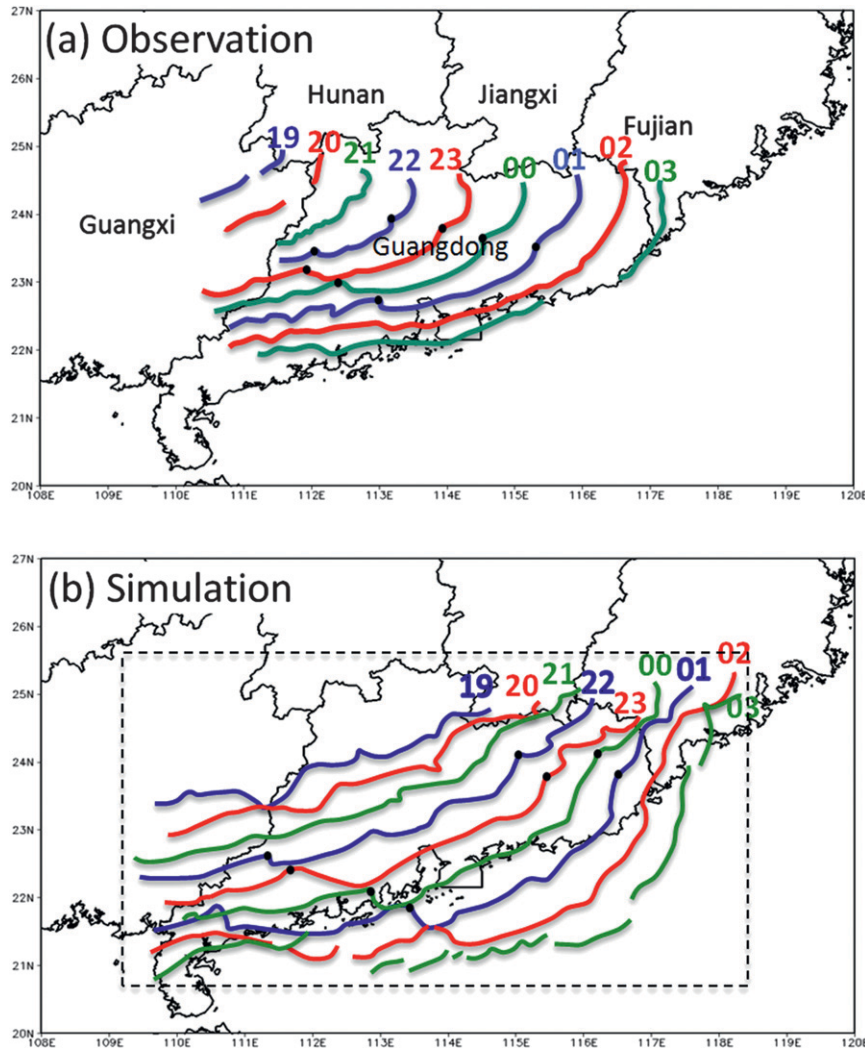


FIG. 2. Isochrones of the (a) observed and (b) simulated squall line. The area of this figure is denoted by the dashed box in Fig. 6. The numbers corresponding to each line are the time of the day (UTC). The dashed box in (b) is the area over which the pressure and potential temperature is averaged for respective perturbation calculation. The segments between the two black dots are the big bow on which this work focuses.

numerical simulations with the Weather Research and Forecasting (WRF) model to examine the formation and evolution of the bowing process for a squall line that occurred on a quasi-stationary front in spring 2007 in South China.

The remainder of this paper is organized as follows. Section 2 summarizes the evolution of the squall line and its synoptic environment, followed in section 3 by an overview of the data and model configuration. The processes responsible for the development of bowing line segments, the associated rear inflow, and bookend vortices are analyzed in section 4. Section 5 contains summary and closing remarks.

2. An observational overview of the squall line and its environment

The squall line of interest originated from scattered clouds in northwestern Guizhou Province along a quasi-stationary front. As shown in the mosaic of composite radar reflectivity based on five S-band Doppler radars in the network of China new generation weather radar (located at the white dots in Fig. 1, including Guilin, Guangzhou, Yangjiang, Shantou, and Xiamen), the individual convective cells merged into a line structure at around 2030 UTC 23 April 2007 near the border between Guangxi and Guangdong Provinces (Figs. 1a,b). A striking feature of

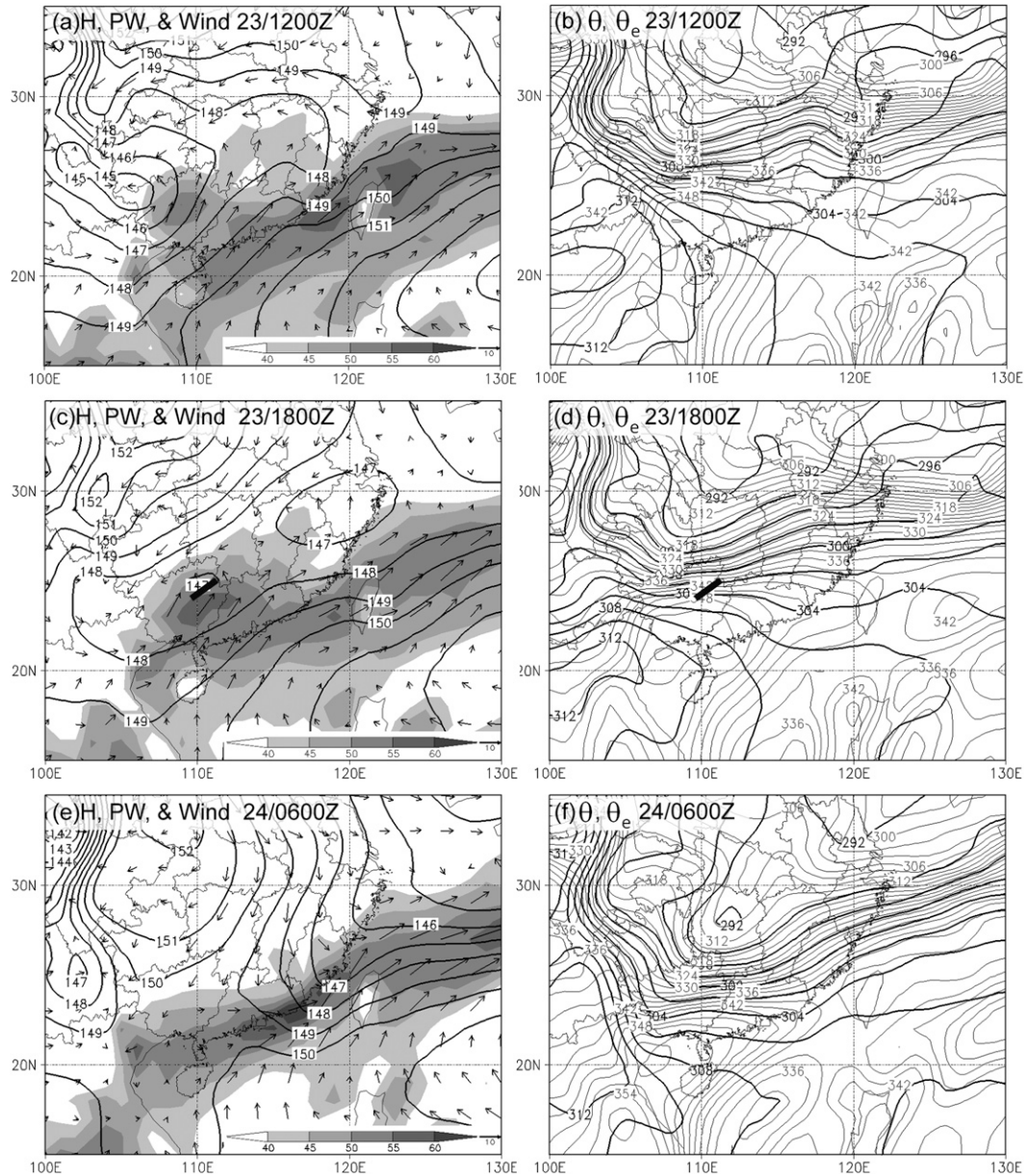


FIG. 3. Environmental features of the squall line based on NCEP FNL analysis. (a),(c),(e) Evolution of geopotential height (black contours every 10 m), ground-relative wind ($m s^{-1}$; the scale is in the bottom-right corner) at 850 hPa, and column-integrated precipitable water (shaded, $kg m^{-2}$) at (a) 1200 UTC 23 Apr, (c) 1800 UTC 23 Apr, (e) 0600 UTC 24 Apr. (b),(d),(f) As in (a),(c),(e), respectively, but for potential temperature (thick contours every 2 K) and equivalent potential temperature (thin contours every 2 K) at 850 hPa. The thick short lines in (c) and (d) denote the position where the squall line took shape 2.5 h later.

the squall line is that two bow-shaped convective segments at 2130 UTC 23 April (marked by double white line arcs in Fig. 1c) expanded and consolidated into a primary bow-shaped convective segment (double white line arcs in Figs. 1c–h). As seen from the isochrones of its leading edge, the observed squall line moved southeastward at a nearly constant speed of $17 m s^{-1}$ (Fig. 2a).

At the early stages of the squall line formation (between 2030 and 2300 UTC), a RIN on the back edge of the stratiform area can be clearly identified with smaller-scale branches pointing to the apex of different bow segments (Figs. 1b–e). The bow segment in the middle of the squall line was about 200 km long at 2300 UTC 23 April (Figs. 1e and 2a), when at least two subsegments

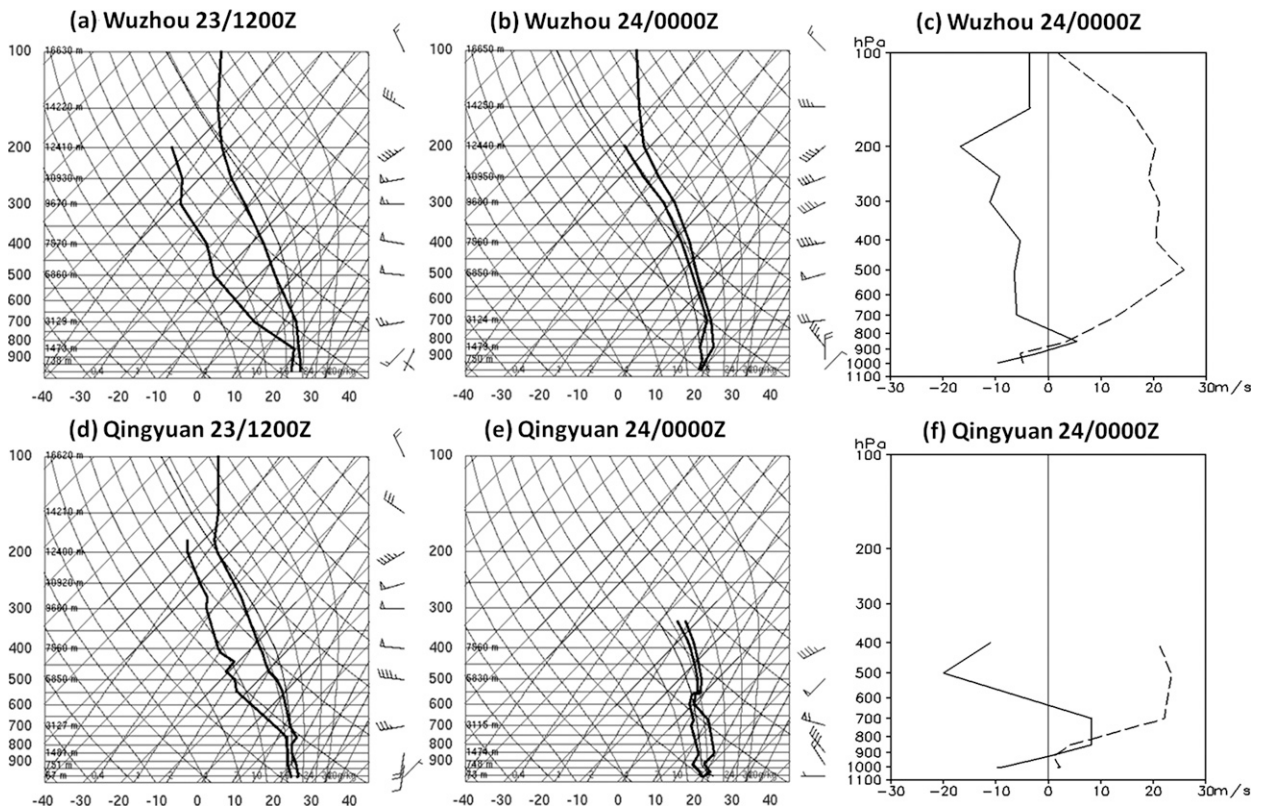


FIG. 4. Skew- T at (a),(b) Wuzhou and (d),(e) Qingyuan radiosonde stations (a),(d) before (1200 UTC 23 Apr) and (b),(e) after (0000 UTC 24 Apr) the squall line passes over the stations. (c),(f) Vertical profile of storm-relative wind normal (solid line) and parallel (dashed line) to the main axis of the squall line at 0000 UTC 24 April to highlight features of rear inflow jet. The locations of these two stations are marked in Fig. 1g.

of bow-shaped echoes were embedded at each end of the large bow. The coexistence of a range of bow-echo scales was also observed in the 5 May 1996 event over the U.S. Great Plains, during which each smaller bow segment had its own rear inflow jet and line-end vortices (Weisman 2001). The squall line started to dissipate at around 0300 UTC 24 April while moving out to sea (Figs. 1j and 2a). This study focuses on the development of the large bowing structure in the middle of the squall line.

The squall line formed in an environment with a well-defined but low-amplitude midlevel trough, a surface quasi-stationary front, and a nocturnal low-level jet. The frontal zone extended from the western part of the Guangxi Province all the way to Japan, with the horizontal wind shear or a convergence zone associated with a leeside low pressure center propagating eastward from the eastern Tibetan Plateau (Figs. 3a,c). The quasi-stationary front had a large meridional gradient of potential temperature but an even larger gradient of equivalent potential temperature θ_e (Figs. 3b,d). Although too early in the season, the front had the characteristics of the mei-yu front (baiu in Japan), which is the most prominent rain producer during the East Asian summer

monsoon (Bao et al. 2011). Mesoscale convective systems during the premonsoon could be even more convective than those during the monsoon, owing to the strong instability over land (Romatschke and Houze 2011).

At 0000 UTC on 23 April, the gradient of θ_e was much weaker over the middle parts of the Yangtze River than over the East China coastal region (not shown). To the south of the large θ_e gradient, the wind at 850 hPa was approximately parallel to the contours of θ_e . In the next 12 h (Figs. 3a,b), the southerly component of the 850-hPa wind intensified in Guangxi Province and advected high- θ_e air northward, thus increasing the gradients of θ_e and temperature across the front. In the meantime, a channel of northerly flow on the cold side of the front started to strengthen and was likely pushing the quasi-stationary front southward. At around 1800 UTC (Figs. 3c,d), the low pressure center in southwestern China extended to the east and northeast and merged with a midlatitude shortwave trough. Further intensification of the northerly flow kept pushing the front southward and southeastward. With the increased convergence between the northerly cold and dry air and southerly warm and moist air, intense convection initiated along the intensifying

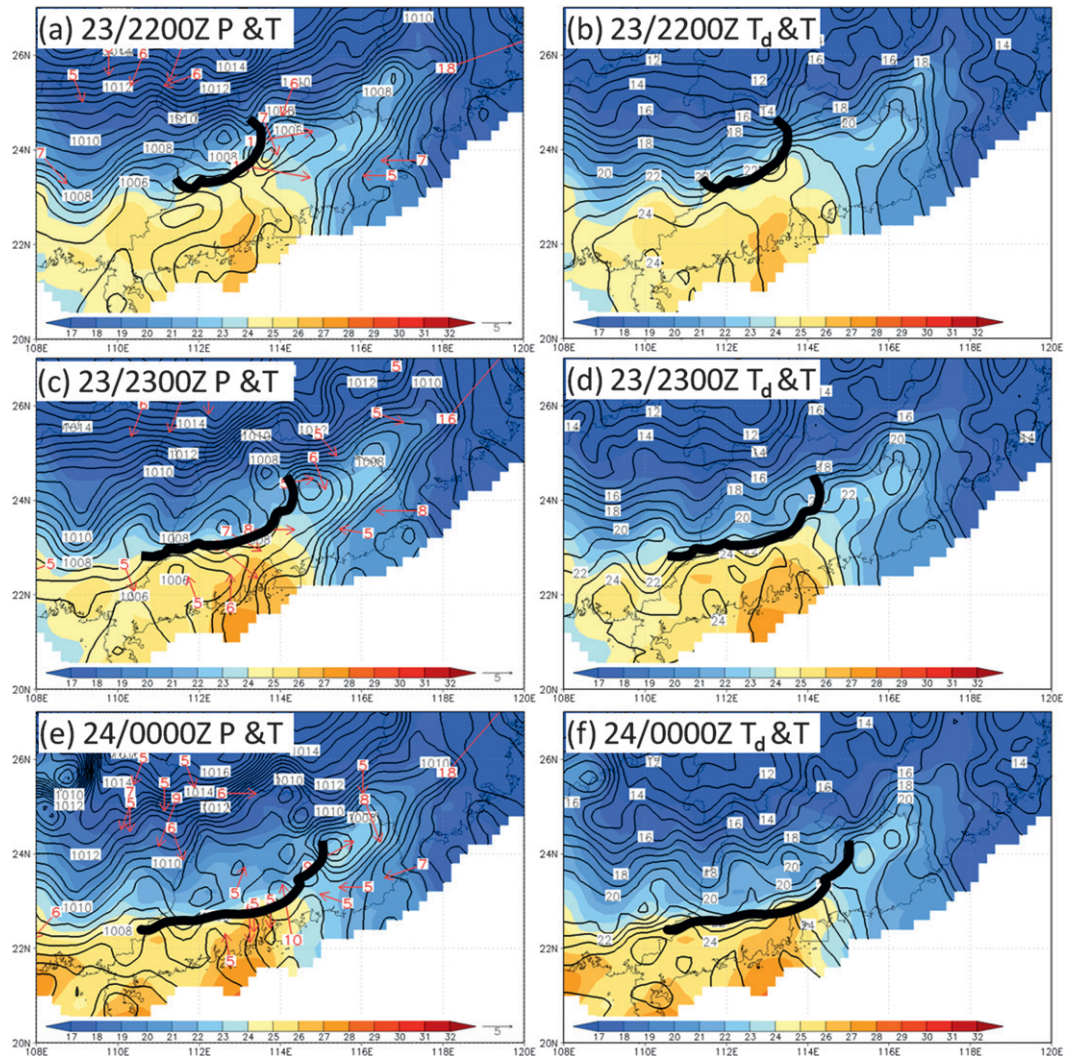


FIG. 5. Sea level pressure (black contours every 0.5 hPa), surface temperature (shaded every 1°C), and surface ground-relative wind stronger than 5 m s^{-1} at (a) 2200 UTC 23 Apr, (c) 2300 UTC 23 Apr, and (e) 0000 UTC 24 Apr. (b),(d),(f) As in (a),(c),(e), respectively, but with the black contour denoting surface dewpoint (every 1°C).

front and rapidly developed into a squall line by around 2030 UTC 23 April over the border regions between Guangdong and Guangxi Provinces (Figs. 1a,b).

The favorable environmental conditions for intense convection were also clearly seen from radiosondes at 1200 UTC 23 April at the Wuzhou and Qingyuan stations (Figs. 4a,d; their locations are indicated in Fig. 1g). Veering winds within the 0–3-km layer were observed with a vertical wind shear of $12\text{--}15 \text{ m s}^{-1}$. The 0–5-km vertical wind shear was $25\text{--}30 \text{ m s}^{-1}$, which is usually regarded as strong (e.g., Weisman and Davis 1998). Values of convective available potential energy (CAPE) from these radiosondes were 1067 and 747 J kg^{-1} , respectively, which are below average for midlatitude cases of squall lines (Bluestein and Jain 1985). This weaker instability is more

common for tropical squall-line environments (Jorgensen et al. 1997). Though not as significant as high CAPE/strong shear, low CAPE/strong shear has also been recognized as an environment in which severe convective systems are likely to occur (Jorgensen et al. 1997).

Because this squall line formed on the southern edge of the frontal zone, surface mesoscale pressure systems associated with the squall line were embedded in the broad subsynoptic surface low associated with the quasi-stationary front. As a result, the mesolows ahead of the squall line—as shown in the surface analyses using the surface observational network of the China Meteorological Administration (Fig. 5)—might not resemble typical presquall lows that result from compensating subsidence (Hoxit et al. 1976; Fritsch and Chappell 1980). Mesolows

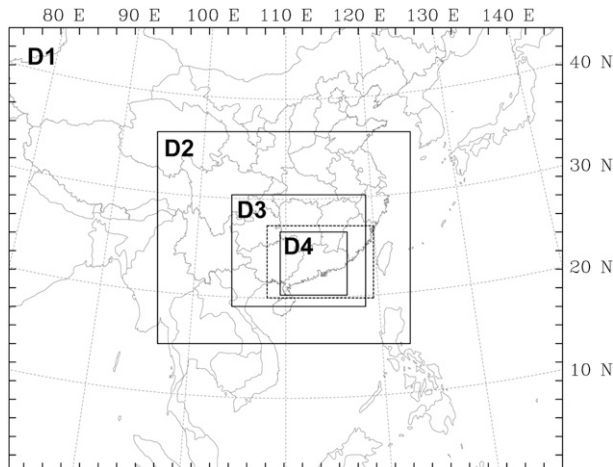


FIG. 6. Model domains. The dashed box denotes the position of Fig. 2.

behind the squall (also known as “wake lows”) appeared at 2200 UTC 23 April (Fig. 5a). A mesohigh pressure center became evident at 2300 UTC 23 April (Fig. 5c), with a closed center appearing 1 h later (Fig. 5e). Because of the nearby quasi-stationary front, the squall-line cold pool did not clearly stand out in

terms of the full temperature field. Surface dewpoint has a gradient similar to temperature with drier air behind the front and moister air in front of it (black contours in Figs. 5b,d,f).

This squall line brought extensive damage to Guangdong Province. A 3-s wind gust of 23.8 m s^{-1} was observed in Guangzhou with 1-h rainfall of 56.6 mm at 0000 UTC 24 April (Chen et al. 2008). The stronger winds along the gust front were basically observed near the apex of the large bowing structure (Fig. 5). This distribution is likely due to the rear inflow behind the bow. Radiosondes at Qingyuan and Wuzhou at 0000 UTC 24 April exhibited backing winds and upper moist/lower dry structure (Figs. 4b,e) typical of a postsquall environment. The line-relative wind component parallel to the line was mostly toward the northeast (Figs. 4c,f). The wind component normal to the line was highlighted by the rear inflow at lower levels with 5 m s^{-1} around 850 hPa at Wuzhou (Fig. 4c) and near 10 m s^{-1} around 800 hPa at Qingyuan (Fig. 4f). The rear inflow seemed to extend higher in altitude and be stronger in intensity from the south to the north. In the following sections, we will examine how the large bowing structure and the attendant rear inflow form, based on a high-resolution numerical simulation.

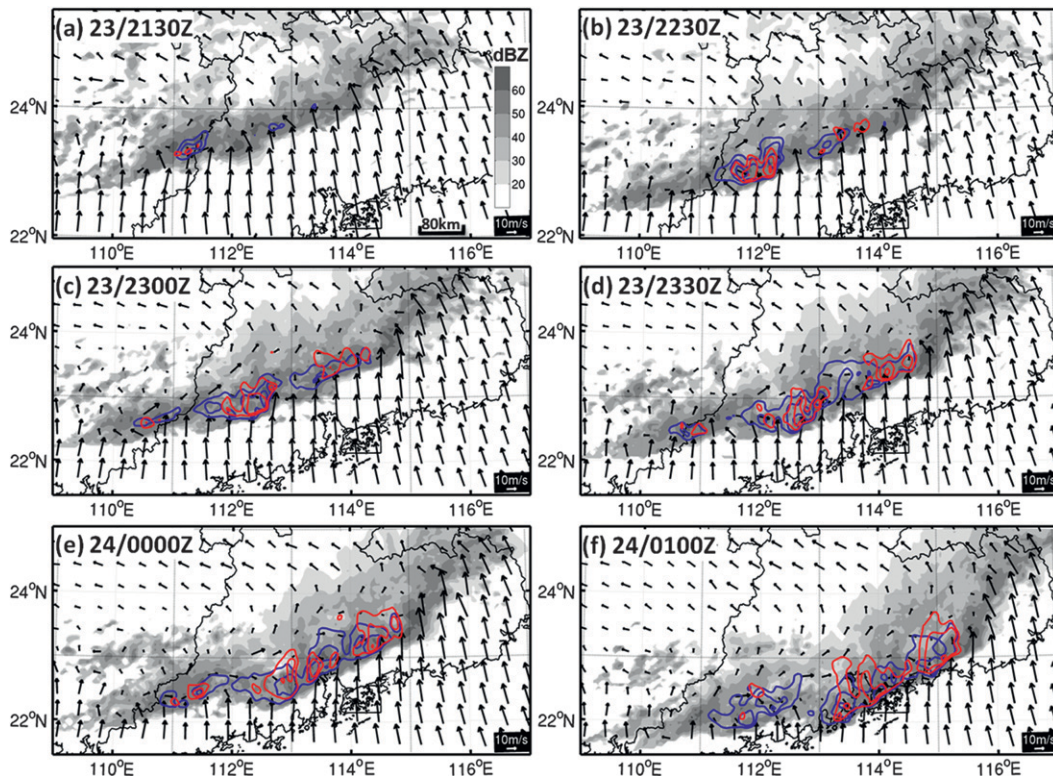


FIG. 7. Simulated evolution of composite radar reflectivity (shaded), line-relative wind vector at 1.5-km height, and rear inflow (the speed of positive line-relative wind component normal to the line) at 1.5 km (blue contours every 4 m s^{-1}) and 2.5 km (red contours every 4 m s^{-1}).

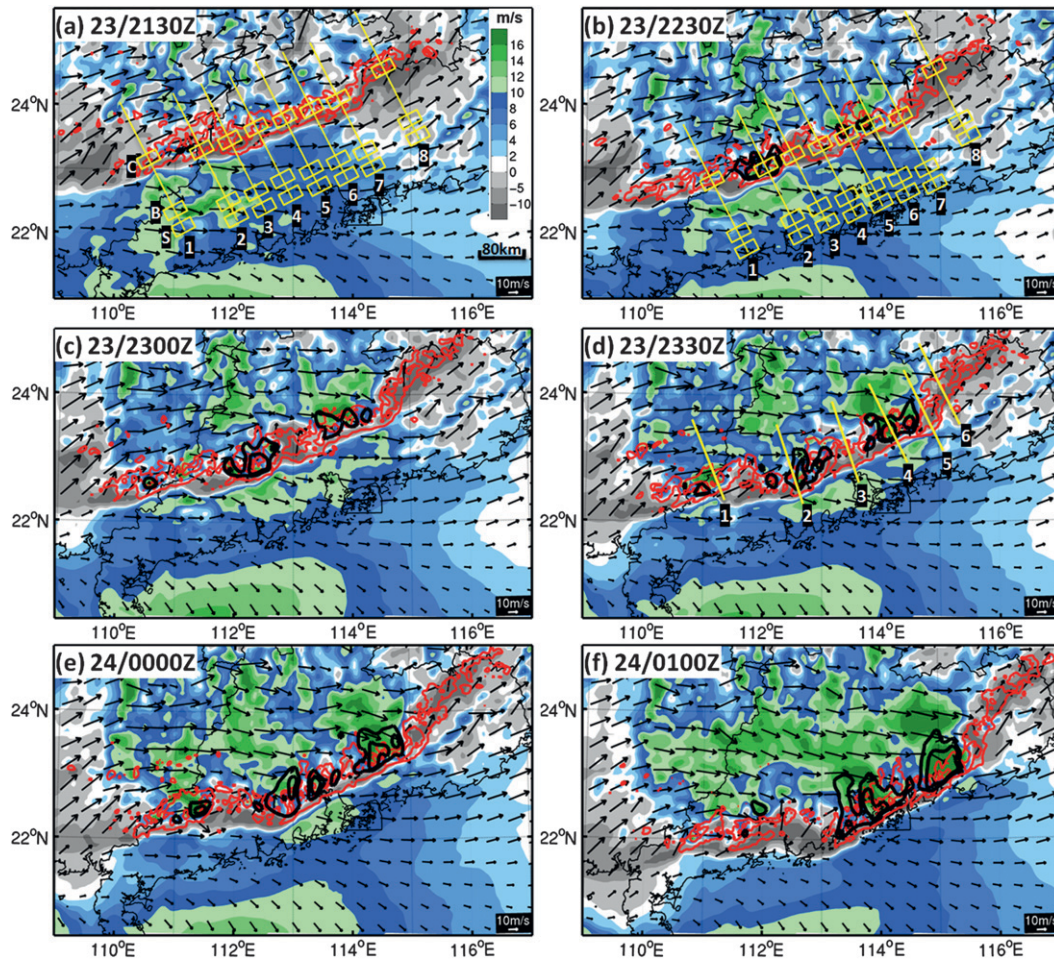


FIG. 8. Simulated evolution of composite radar reflectivity (red contours for 50 and 60 dBZ), vertical wind shear vector between 0.25 and 3 km and its component normal to the leading edge of squall line (shaded; blue and green for forward and gray for backward), rear inflow (the speed of positive line-relative wind component normal to the line) at 2.5 km (black contours for 4 and 8 m s^{-1}). The yellow line and rectangles are the geometry used in the calculation of virtual potential temperature and buoyancy perturbation as well as the vertical wind profile normal to the leading edge of the squall line. Letters S and B denote the area used to calculate the averages of environmental wind and virtual temperature, respectively, and letter C is for the average of virtual temperature and condensates of the cold pool.

3. Numerical model and configurations

The data used in this work include conventional surface and radiosonde observations, final analysis data (FNL) from the National Centers for Environmental Prediction (NCEP), and radar data in southeastern China.

The numerical experiment was performed using WRF v3.2 (Skamarock et al. 2008) with four domains and two-way nesting (Fig. 6). The domains have 35 vertical layers with the model top at 10 hPa and 150×120 , 205×172 , 316×205 , and 481×451 grid points in the horizontal with gridpoint intervals of 40.5, 13.5, 4.5, and 1.5 km, respectively. The model was integrated for 24 h starting at 1200 UTC 23 April 2007 with the initial and boundary conditions provided by 6-hourly FNL NCEP analysis of $1^\circ \times 1^\circ$. Physical parameterization schemes include the

WRF single-moment (WSM) six-class microphysics scheme with graupel (Hong et al. 2010), the Yonsei State University (YSU) scheme (Noh et al. 2003) for planetary boundary layer processes, and the Grell–Devenyi cumulus scheme (Grell and Devenyi 2002) for the 40.5- and 13.5-km domains (no cumulus parameterization scheme was used for 4.5- and 1.5-km domains).

4. Results from the numerical simulation

a. Model-simulated bowing processes and associated rear inflow of the squall line

The basic features of the squall line (orientation, propagation, and structure) and the formation of the large bowing structure (the bow segment between the two black

TABLE 1. The cold pool and environment parameters at 2130 and 2230 UTC 23 Apr at cross sections 1–8 along the squall line as marked in Figs. 8a,b: H is the cold pool depth (km AGL) defined as $\theta'_v(H) \leq -1$ K, c is theoretical cold pool speed, and Δu_{\max} (m s^{-1}) is the maximum vertical shear normal to the cold pool through its depth. The mean value over 2–7 denotes the general features of the bowing part.

Parameter	Time (UTC)	1	2	3	4	5	6	7	8	Mean of 2–7
c (m s^{-1})	2130	26.5	34.9	32.5	31.8	29.4	28.4	25.5	25	30.4
	2230	27.7	36.7	31.1	32.5	34.1	33.0	28.9	25.6	32.7
H (km)	2130	2.7	3.5	3.8	3.9	3.9	3.8	3.6	2.8	3.8
	2230	3.0	4.1	3.3	3.8	4.1	4.2	3.7	3.9	3.9
Δu_{\max} (m s^{-1})	2130	10.2	14.3	14.4	12.7	11.5	11.3	10.2	4.6	12.4
	2230	10.6	15.7	12.6	13.2	15.3	14.2	10.4	9.5	13.6
$c/\Delta u_{\max}$	2130	2.6	2.4	2.3	2.5	2.6	2.5	2.5	5.4	2.5
	2230	2.6	2.3	2.5	2.5	2.2	2.3	2.8	2.7	2.4

dots in Fig. 2) are generally well simulated by the WRF model, except that the simulated squall is initiated a couple of hours earlier than observed (and thus is always positioned ahead of the observed in sequent hours) and has a larger extent in length at the beginning (cf. Figs. 2b and 2a). The simulated squall line forms while the cold pools and gust fronts of several cloud clusters expand and merge into a northeast–southwest-oriented line in northeastern Guangxi Province at about 1700 UTC 23 April. Convection on the southern end of the squall line continues to develop and strengthen, which eventually evolves into a continuous line of approximately 400 km with reflectivity greater than 40 dBZ by 2100 UTC 23 April (Fig. 2b). The simulated squall line moves at a speed of 16 m s^{-1} along a heading of 135° , which is very close to the observed 17 m s^{-1} along a heading of 115° . Several bow segments first develop in the middle portion of the squall line and eventually merge into a coherent large bowing structure at 2300 UTC. The large bow continues to push forward until 0100 UTC 24 April, then dissipating gradually after moving out to sea (Fig. 2b). We will examine the formation mechanism of this large bowing structure based on the model output of the 4.5-km domain (instead of the 1.5-km domain) because our emphasis is on the storm-scale features (rather than the structure of individual convective cells), which are generally similar in both domains except that there is much more noise in the 1.5-km domain.

The simulated radar reflectivity, rear inflow (greater than 4 m s^{-1}) at 1.5 and 2.5 km, and line-relative winds at 1.5 km are illustrated in Fig. 7. The line-relative winds are obtained by subtracting the mean squall-line moving speed averaged during this period from the total winds. The rear inflow is the projection of the line-relative winds onto the direction normal to the long axis of the squall line. The rear inflow appears first at lower levels on the southern part of the squall line (blue contour in Fig. 7a). Only a weak rear inflow (no stronger than 4 m s^{-1}) is simulated at 2.5 km at this time (red contour in Fig. 7a). Two other much smaller rear inflow patches

of 4 m s^{-1} appear more to the north (at about 112.8° and 113.2°E) at 1.5 km. The rear inflow strengthens and expands both horizontally and vertically at 2230 UTC (Fig. 7b). As a result, the areas with the strongest rear inflows start bowing. At both ends of the squall line, the line-relative wind field is characterized by contiguous front-to-rear flows that will slow the movement of both ends and thus enhance the bowing process.

The rear inflow jets expand farther in the following hours (Figs. 7c–f). The southern patches of the rear inflow have a comparable extent at 1.5 and 2.5 km (but are stronger at 1.5 km; see Fig. 7d), while the extent and intensity of the northern patches of the rear inflow is larger at 2.5 km than at 1.5 km, which is generally consistent with the difference in the height of the rear inflow observed in the Qingyuan and Wuzhou radiosondes at 0000 UTC 24 April (Figs. 4c,f). The greater-than- 4 m s^{-1} rear inflow in the northern and southern parts of the squall lines expands laterally toward each other and eventually merges into one contiguous zone of rear inflows by 2330 UTC 23 April at 1.5 km (Fig. 7d). The rear inflows at 2.5 km stay separate until the squall line starts dissipating at 0100 UTC 24 April (Fig. 7f). The RINs are seen behind the maximum rear inflow (e.g., 23°N , 112.5°E in Fig. 7d). Likely forced by the rear inflow zone, the middle part of the squall line bows out possibly because of the acceleration in convection propagation and/or advection. This result indicates that the formation, intensification, and expansion of the rear inflow are essential to the formation of the large bow-shaped convective segment within the squall line.

b. The formation mechanism of the large bowing structure

1) THE IMPACT FROM THE COLD POOL AND ENVIRONMENTAL VERTICAL SHEAR

The bowing structure is actually the result of part of the squall line moving faster than its neighboring parts. The moving speed of a squall line is closely related to the

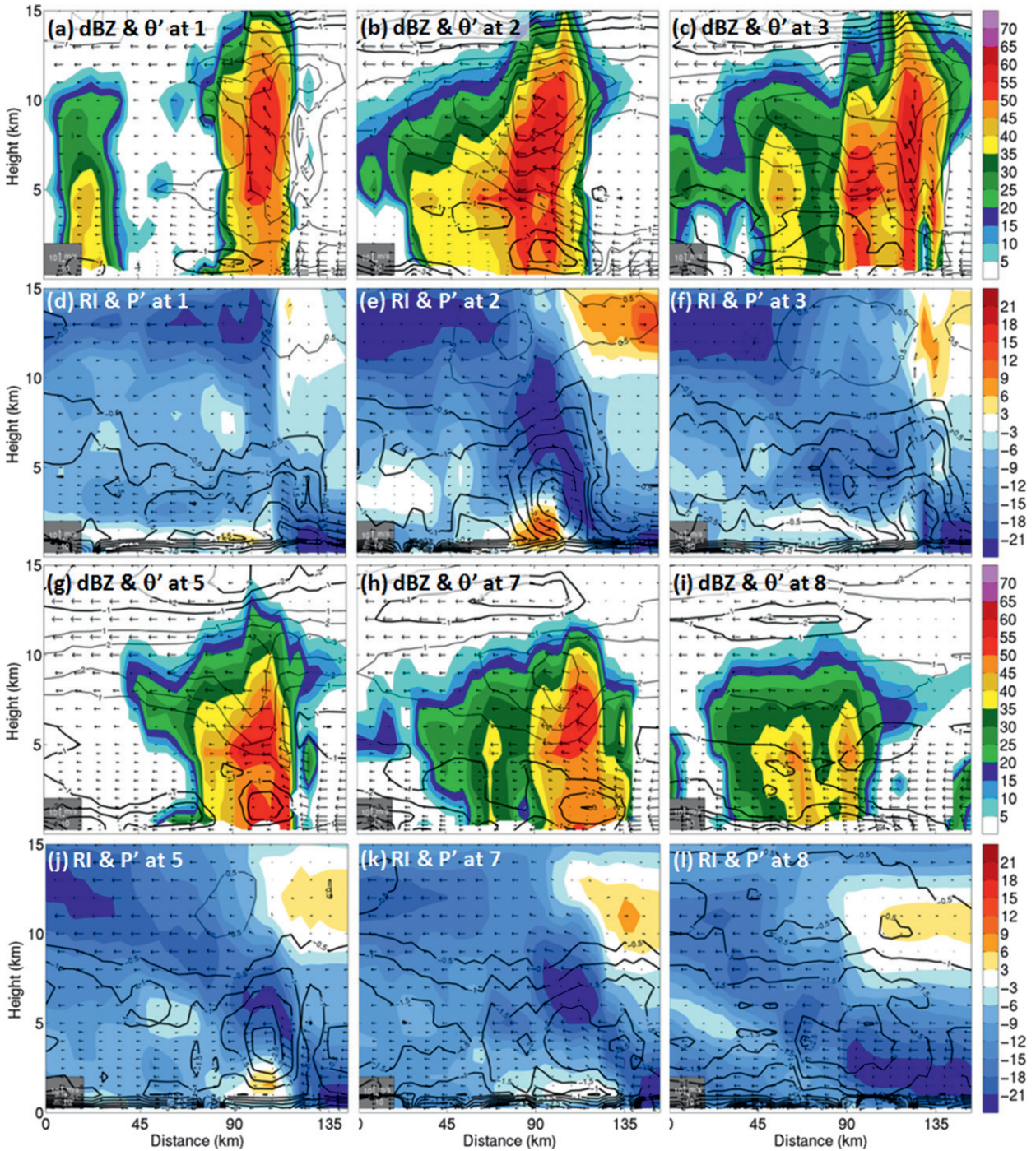


FIG. 9. Vertical cross sections of radar reflectivity, line-relative wind component, and potential temperature perturbation (black contours; thin for positive and thick for negative; every 1 K) at 2130 UTC 23 Apr 2007 along lines (a) 1, (b) 2, and (c) 3 as denoted in Fig. 8. (d)–(f) The corresponding rear inflow (wind vector projected onto the cross section and speed as shaded at an interval of 3 m s^{-1}) and pressure perturbation (black contours, thin for positive and thick for negative; every 0.5 hPa). (g)–(l) As in (a)–(f), but for the cross sections along lines (g),(j) 5, (h),(k) 7, and (i),(l) 8.

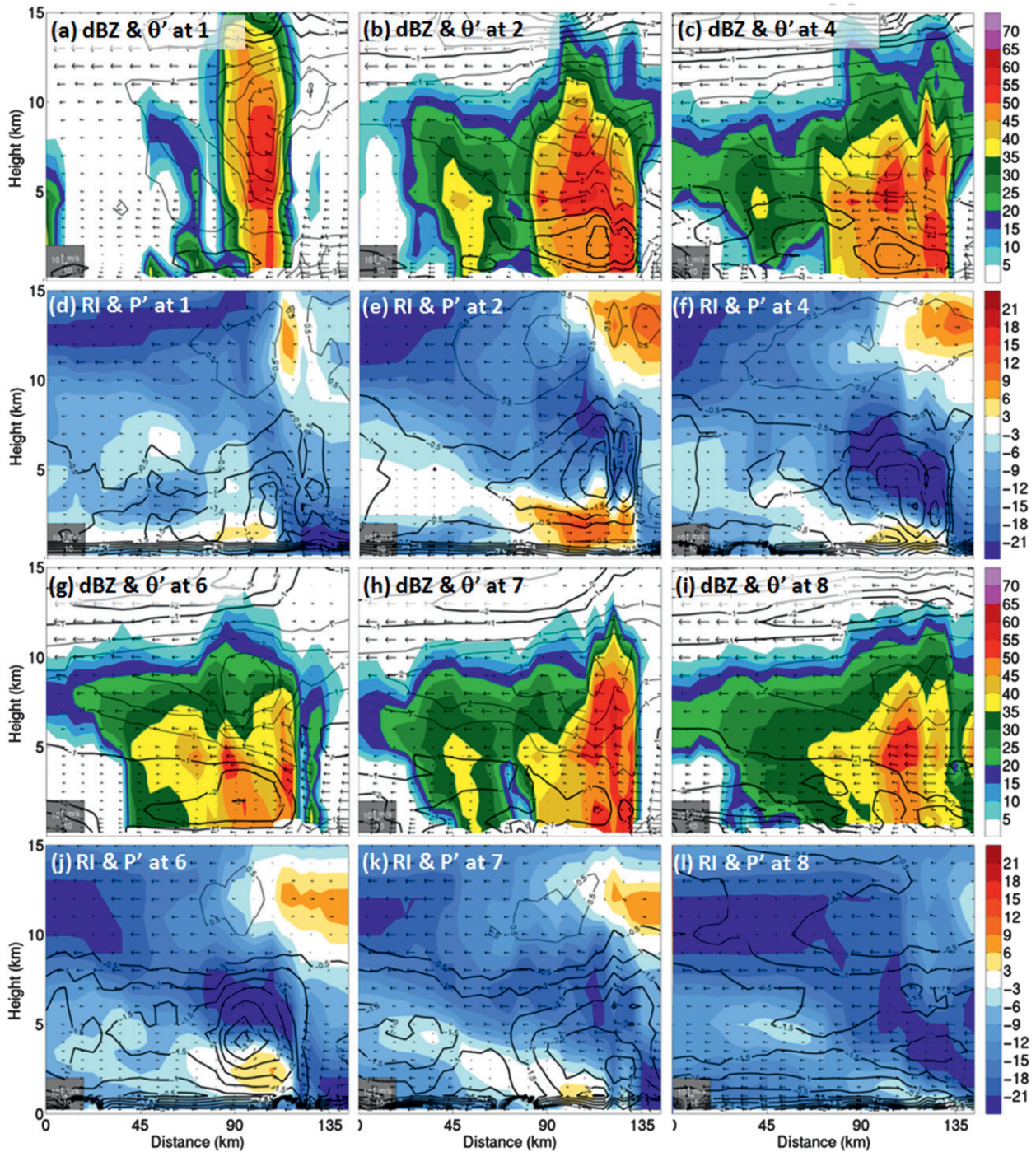


FIG. 10. As in Fig. 9, but for 2230 UTC 23 Apr.

intensity of the cold pool. The relationship between the bowing structure and the intensity or the theoretical speed of cold pool c is examined in this section. As in previous works (e.g., Rotunno et al. 1988; Trier et al. 2006; Meng and Zhang 2012), the theoretical speed of cold pool is calculated by

$$c^2 = -2 \int_{z=0}^{z=H} B dz, \quad (1)$$

where B is the total cold pool buoyancy including contributions from virtual potential temperature perturbations θ'_v and the mixing ratio of all condensate q_c , defined

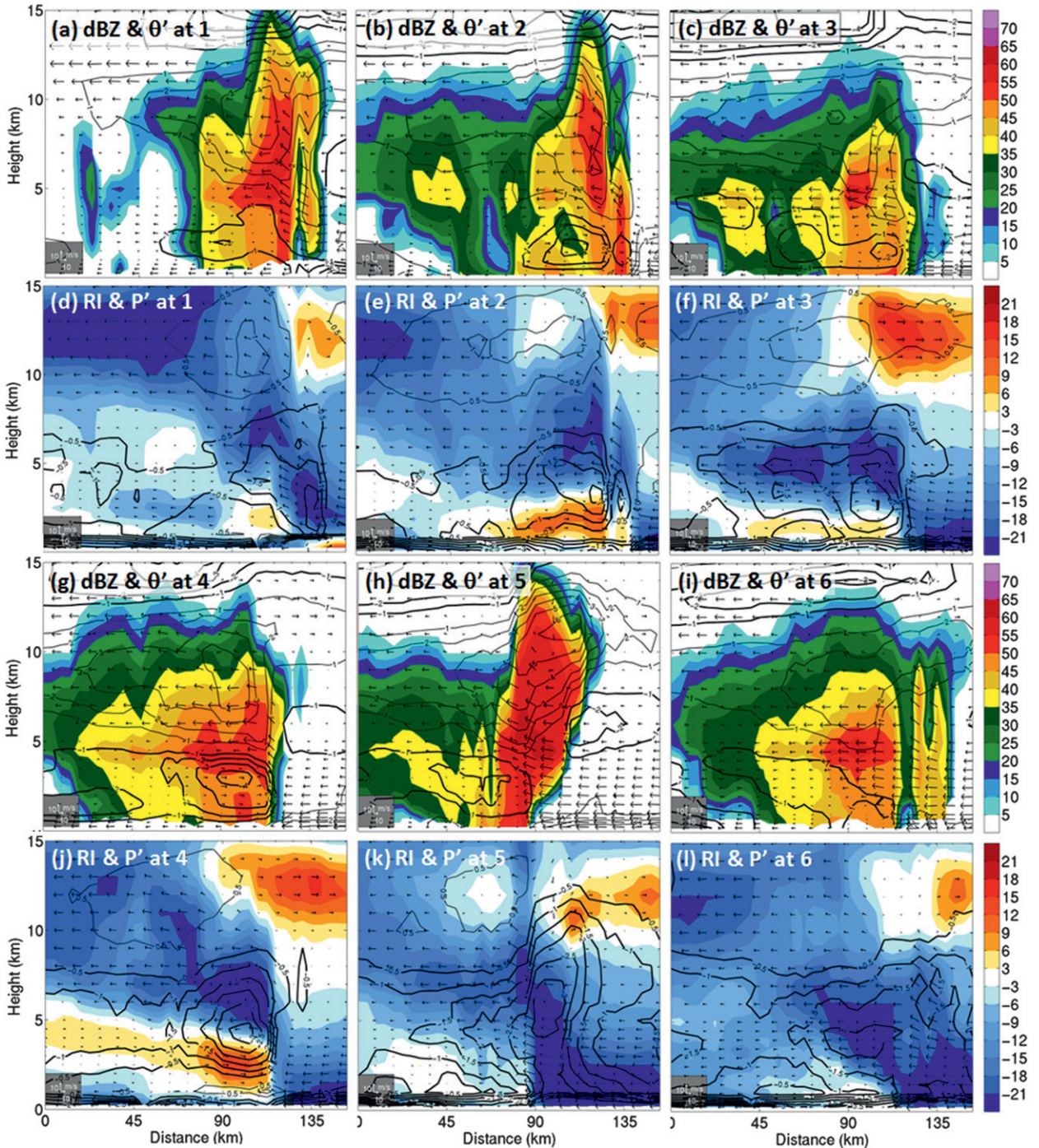


FIG. 11. As in Fig. 9, but for 2330 UTC 23 Apr.

as $B = g(\theta'_v/\bar{\theta}_v - q_c)$, where $\bar{\theta}_v$ is the environmental virtual potential temperature. The method we used to calculate H , the depth of the cold pool, is different from that used in Trier et al. (2006). We used the depth of the layer where $\theta'_v(H) \leq -1$ K instead of $B(H) \leq 0$ because the vertical gradient of B near zero has a very large variability

and may result in an unreasonably deep cold pool. Here $\bar{\theta}_v$ is calculated as an average of virtual potential temperature over a rectangular area 70 km ahead of the gust front with a length (width) of 40 (20) km in the direction parallel (normal) to the gust front (e.g., area B in Fig. 8a). The averaged virtual potential temperature in the cold

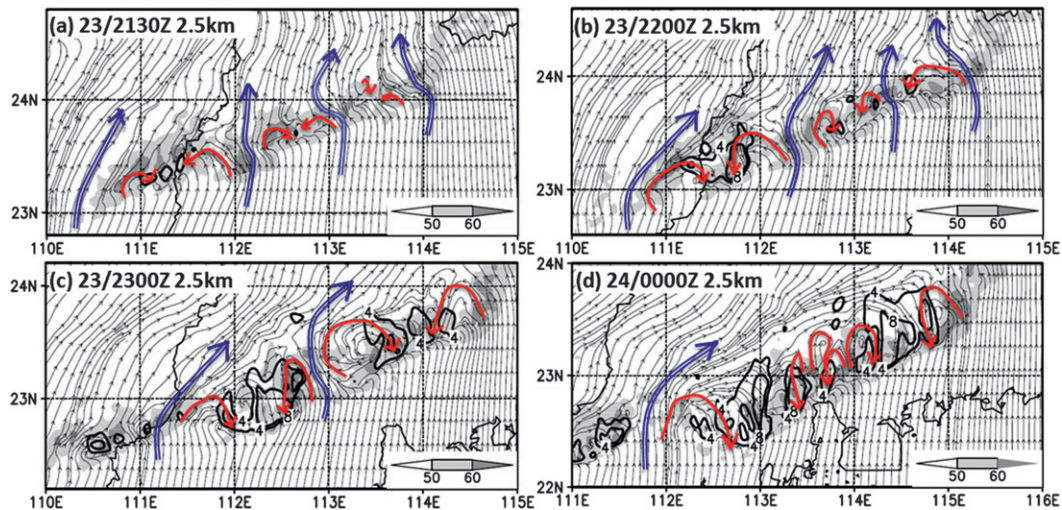


FIG. 12. Evolution of line-relative streamline at 2.5 km together with composite radar reflectivity (shaded, dBZ) at (a) 2130 UTC 23 Apr, (b) 2200 UTC 23 Apr, (c) 2300 UTC 23 Apr, and (d) 0000 UTC 24 Apr. The black contour denotes the rear inflow (every 4 m s^{-1}). The double blue arrows represent front-to-rear flow. The red curved arrows denote bookend vortices.

pool $\bar{\theta}_c$ is an average of virtual potential temperature calculated at all points within an area 10 km behind the gust front with a length (width) of 40 (20) km in the direction parallel (normal) to the gust front (e.g., area C in Fig. 8a). The perturbation virtual potential temperature is then obtained by $\bar{\theta}_c - \bar{\theta}_v$. Note that q_c is calculated in the same way as $\bar{\theta}_c$. The intensity c and height H of the cold pool were calculated at eight positions along the squall line (Figs. 8a,b), with positions 1 and 8 located at the southern and northern ends of the squall line, respectively, and positions 2–7 uniformly distributed along the part where the big bowing structure develops for 2130 (Fig. 8a) and 2230 UTC (Fig. 8b) 23 April (Table 1). The cold pool is stronger or faster as shown by c and higher as shown by H where the bowing structure develops than in the two ends of the squall line as shown by both the individual values at positions 2–7 and their average. Within the range of the bowing structure, the cold pool is stronger in the southern part than in the northern part. From 2130 to 2230 UTC, the cold pool intensified by about 2.5 m s^{-1} in the bowing part but did not change much at the two ends of the squall line, especially in the northern end.

Environmental vertical shear is another important factor that determines where the squall line tends to propagate. The 0.25–3-km vertical shear that is normal to the gust front of the squall line (hereafter referred to as Δu) is depicted at different times (shaded in Fig. 8). Figure 8 shows that the maximum value of Δu (green shading denotes the area where $\Delta u > 10 \text{ m s}^{-1}$) ahead of the gust front appears first at 2130 UTC 23 April near 22°N , $111^\circ\text{--}112^\circ\text{E}$ where the southern part of bowing structure starts to develop. It weakens gradually northward and becomes

negative (gray shading) even in the northern end of the squall line. Associated with the stronger Δu , rear inflow appears right behind the southern part of the leading edge. Over the next 2.5 h, Δu expands more to the north forming a band of Δu larger than 10 m s^{-1} in front of the squall line. This large environmental shear band is well collocated with the position of the large bowing structure.

According to Rotunno et al. (1988), the optimum condition that maximizes the gust front updraft is that the environmental vertical shear normal to the gust front over roughly the depth of the cold pool¹ is equal and opposite to the horizontal vorticity baroclinically generated by cold pool, which can be expressed by $c/\Delta u = 1$. This hypothesis has been further confirmed by Weisman and Rotunno (2004) through a 3D simulation with a higher resolution and a larger range of environmental shear conditions than those in Rotunno et al. (1988), and it is also supported by a multimodel assessment (Bryan et al. 2006). Using the same geometry as that in Trier et al. (2006, their Fig. 9), the wind component normal to the gust front is calculated 100 km ahead of the gust front (e.g., the area S in Fig. 8a). The ratio $c/\Delta u_{\text{max}}$ is examined at cross sections 1–8 along the squall line at 2130 and 2230 UTC (Δu_{max} is the maximum value of the average vertical shear over the box S between different

¹ Strictly speaking, it is the shear over the depth of the control volume; the top of the control volume used by Rotunno et al. (1988) was chosen here to be the height at which the control volume–relative wind vanished at the top rear and top forward corners of the volume. This altitude is slightly higher than the mean height of the cold pool.

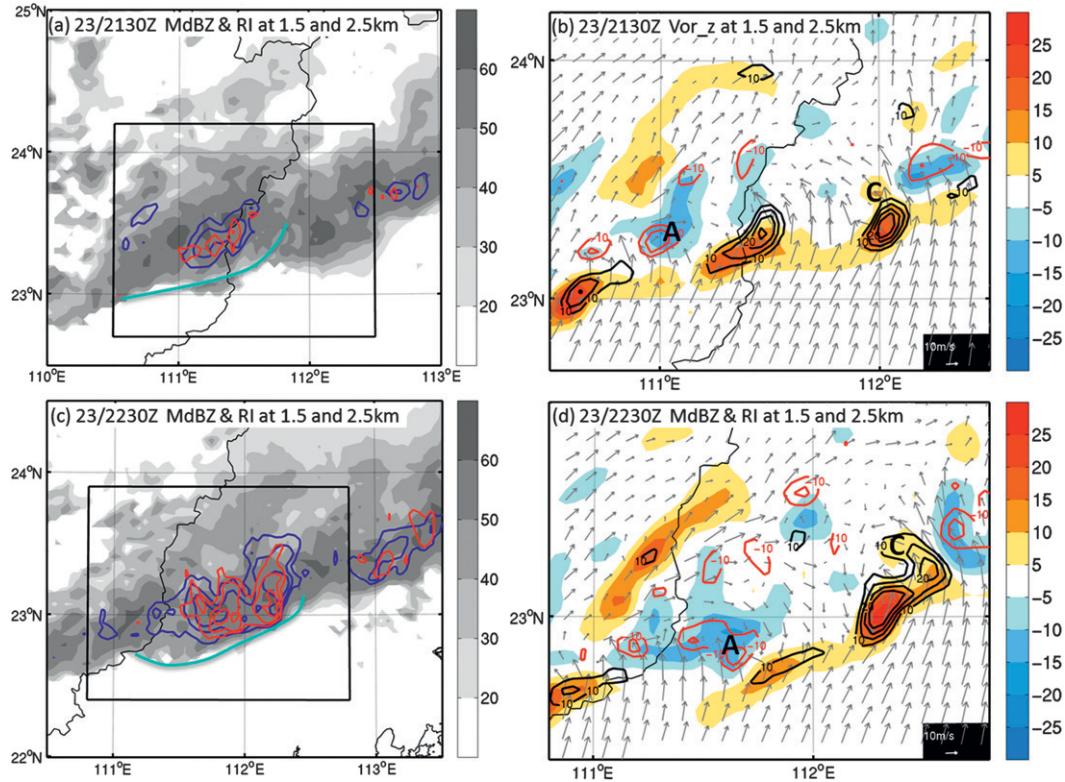


FIG. 13. Vertical vorticity analysis for the southern bow segment at (a),(b) 2130 UTC 23 Apr and (c),(d) 2230 UTC 23 Apr. (a),(c) Shading indicates composite radar reflectivity (dBZ); the contours denote the speed of positive line-relative wind component normal to the line at 1.5 (blue contour) and 2.5 km (red contour) at an interval of 4 m s^{-1} . (b),(d) Vertical vorticity (every $5 \times 10^4 \text{ s}^{-1}$, starting from $10 \times 10^4 \text{ s}^{-1}$) at 1.5 km (shaded, warm colors for positive and cool colors for negative) and 2.5 km (contours, black lines for positive and red lines for negative) as well as the line-relative flow at 2.5 km in the solid boxes in (a) and (c), respectively. The cyclonic and anticyclonic centers are indicated by letters C and A.

levels through H). Similar to the results of Meng and Zhang (2012), the ratios of $c/\Delta u_{\max}$ are between 2 and 3 (i.e., larger than 1). This suboptimal condition might have contributed to the dominant trailing stratiform organization. The averaged ratio of $c/\Delta u_{\max}$ is closer to 1 where the bowing structure develops, relative to those in area 1 and 8 at the ends of the squall line and get even closer to 1 from 2130 to 2230 UTC. The ratio is closest to 1 near the location of rear inflow, which indicates that better balance between the cold pool and environmental vertical shear may have helped the development of the bowing structure.

2) THE FORMATION MECHANISM OF REAR INFLOW ASSOCIATED WITH THE LARGE BOWING STRUCTURE

Rear inflow could be forced by various factors such as environmental flow, midlevel pressure deficit, and bookend vortices. The impact of the environment flow on the rear inflow jet is first examined. The line-relative

flow near the back edge of the stratiform region nearly points against the rear inflow (Fig. 7), suggesting that the ambient flow does not produce the rear inflow in this case, which is similar to what was observed by Grim et al. (2009) in their case.

The impact of pressure gradient associated with the midlevel pressure deficit due to vertical gradient of buoyancy is also minor in this case. At 2130 UTC 23 April, the potential temperature perturbation, pressure perturbation, radar reflectivity, and squall-relative wind along six vertical cross sections, denoted by the lines 1, 2, 3, 5, 7, and 8 in Fig. 8a, are examined (Fig. 9). The pressure perturbations are calculated by subtracting the horizontally averaged pressure over the dashed box in Fig. 2b (the box covers the entire life cycle of the squall line) from the full pressure fields at each level. It is clear that the distributions of all these variables are highly uneven along the squall line. Lines 1 and 8 represent the ends of the squall line, beyond where the bowing structure develops. Both of these cross sections show front-to-rear flow almost at

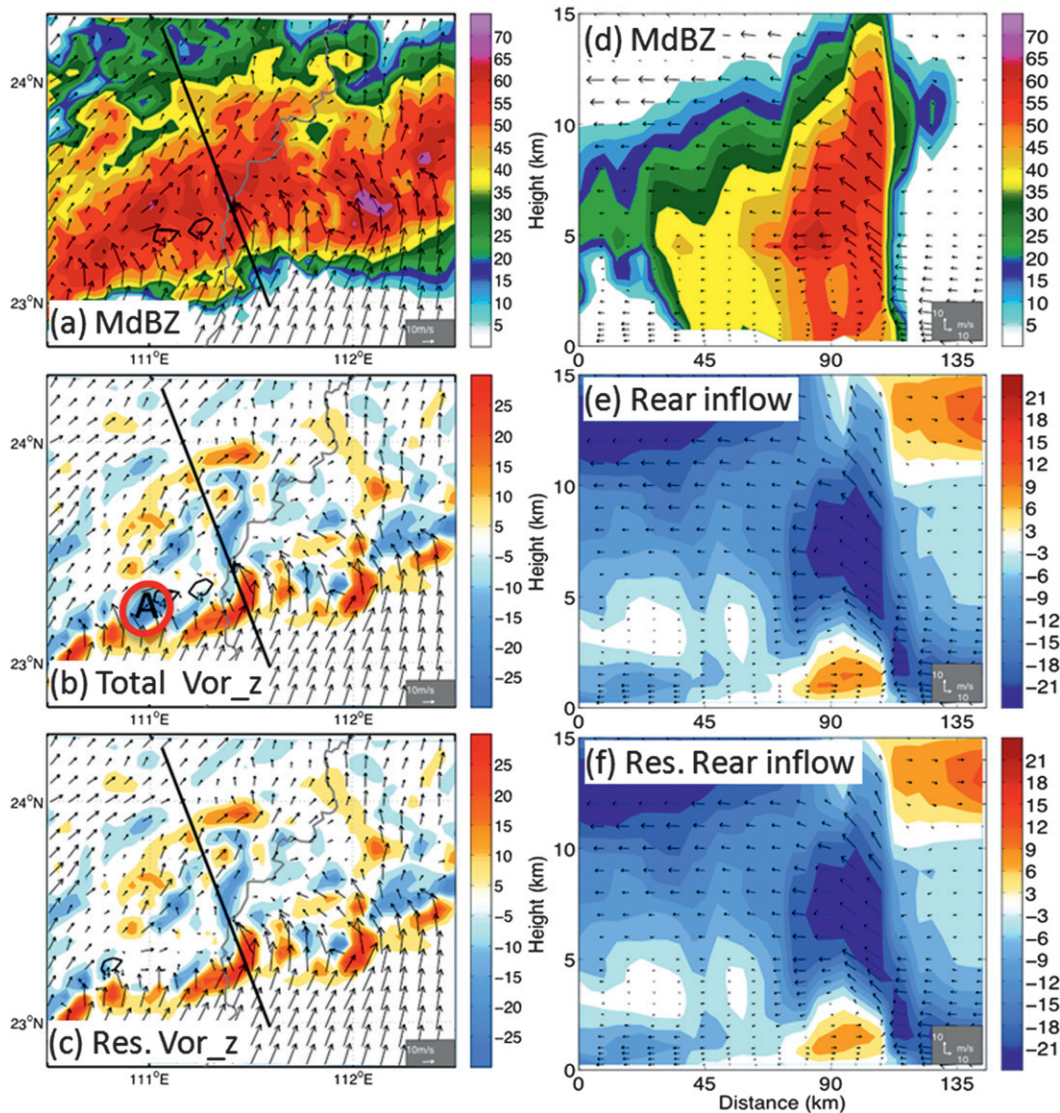


FIG. 14. The contribution of bookend vortices to the rear inflow in the southern part at its developing stage at 2130 UTC 23 April. (a) The composite radar reflectivity (shaded, dBZ), line-relative wind vector (m s^{-1}), and the rear inflow speed at 2.5 km (every 4 m s^{-1}). (b) As in (a), but the shading denotes the vertical vorticity at 2.5 km (every $5 \times 10^4 \text{ s}^{-1}$). The red circled area denotes the anticyclonic center. (c) As in (b), but with the anticyclonic vorticity and its associated flow removed. (d)–(f) Cross sections along the thick lines in (a)–(c) of wind and radar reflectivity [shaded in (a)] and wind speed projected to the cross section [shaded in (e) and (f)]. The cyclonic and anticyclonic centers are indicated by letters C and A.

all levels behind the gust front (Figs. 9d,l). Rear inflow is stronger and higher at lines 2 (Fig. 9e) and 5 (Fig. 9j). Lines 3 and 7 denote the areas in the bowing structure that do not have apparent rear inflow, especially at upper levels (Fig. 8a). Within the extent where the bowing structure develops (cross sections at lines 2, 3, 5, and 7), strong low pressure perturbations are seen where there are positive (negative) potential temperature perturbations above (below). Stronger rear inflow accompanies stronger low-pressure deficits. However, instead of where there are

large horizontal gradients of pressure perturbation (such as the area to the left of the deficit center), the rear inflow mainly appears in the lower half of the closed contours of the low-pressure perturbation in the cross sections where the pressure gradient are generally weaker. Similar results are seen at 2230 (Fig. 10 at lines 2, 4, 6, and 7) and 2330 UTC 23 April (Fig. 11 at lines 2, 3, 4, and 5). This result suggests that the midlevel pressure gradient associated with the pressure deficit may not be a key factor to force the rear inflow. Considering that the stronger rear inflow in

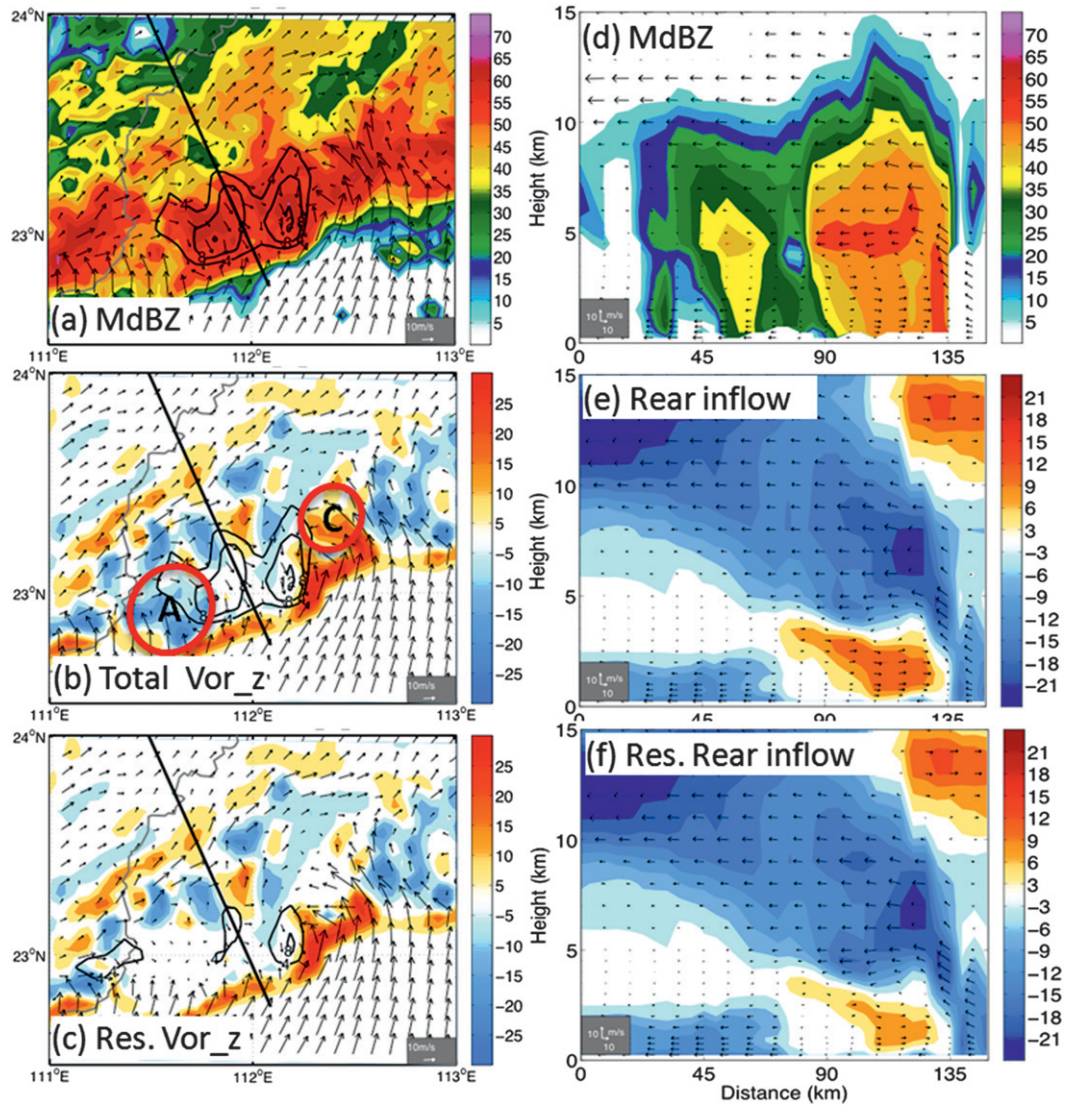


FIG. 15. As Fig. 14, but at 2230 UTC 23 Apr.

Figs. 9–11 usually has a larger vertical extent with a higher level of the maximum, a possible contributor to the rear inflow especially at upper levels could be bookend vortices.

(i) *The impact from the consolidation of multiple bookend vortices*

Observational study shows that bookend vortices may account for 50% of the rear inflow at the initial stage, with the percentage tending to increase later on (Grim et al. 2009). In this case, three pairs of bookend vortices become apparent in the middle segment of the large bow at around 2130 UTC 23 April (Fig. 12a). The 2.5-km streamline plot shows that the three pairs of anticyclonic and cyclonic circulations are closely associated with four

channels of front-to-rear line-relative flow situated near 110.5°, 112.2°, 113.2°, and 113.8°E, at intervals of roughly 100 km. The southernmost pair of bookend vortices is better organized than the other two pairs. Rear inflow is seen between the southern and middle pairs of bookend vortices.

In the next 30 min, the southern bookend vortices become even better organized with a wider area of rear inflow (Fig. 12b). The middle two front-to-rear flow channels shrink in width along the line, associated with which is the obvious growth of the distance between the vortices in each of the southern two pairs of bookend vortices with a better and larger organized anticyclonic center. The leading edge of active convection substantially bows out where the local maxima of rear inflow are located between

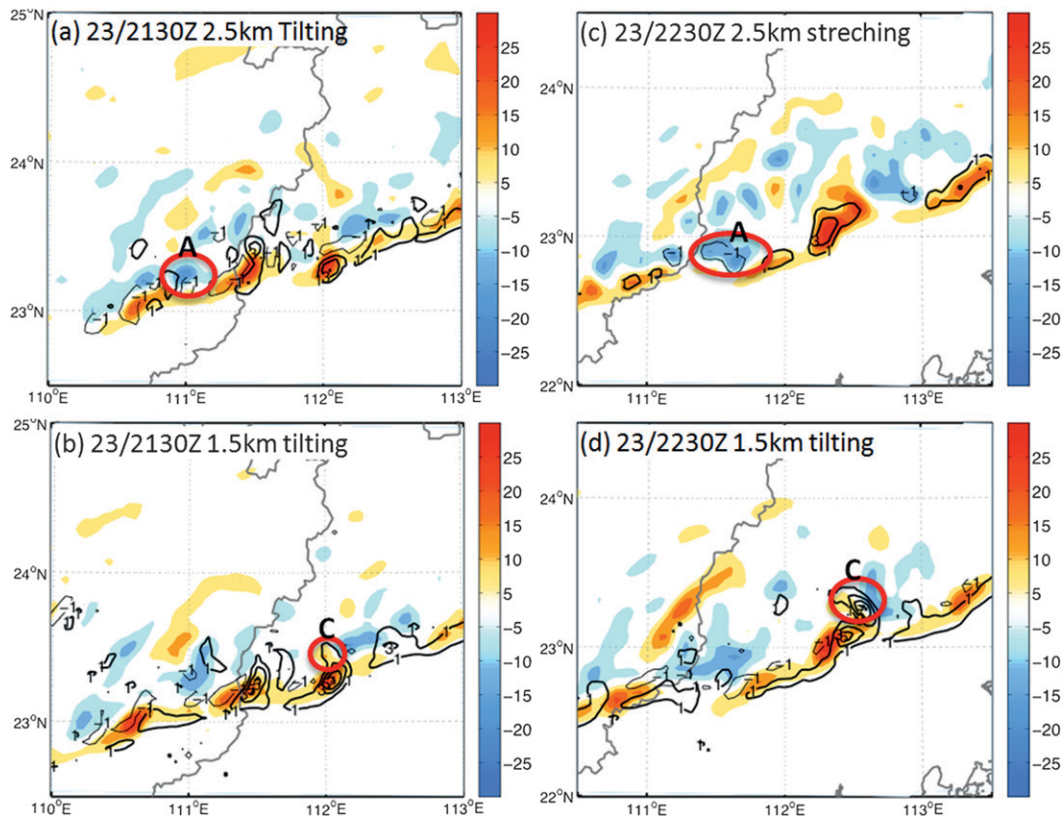


FIG. 16. The formation of bookend vortices. (a),(c) The vertical vorticity (shaded, every $5 \times 10^{-4} \text{ s}^{-1}$) at 2.5 km, and (a) the tilting terms (contours, every $2 \times 10^{-8} \text{ s}^{-2}$) at 2130 UTC 23 April and (c) stretching terms (contours, every $2 \times 10^{-8} \text{ s}^{-2}$) at 2230 UTC at the same level, with thick contours for positive and thin contours for negative. The red circle denotes the anticyclonic vortex of the bookend vortices. (b),(d) As in (a),(c), but for 1.5 km; both contours denote tilting terms with the red circle denoting the cyclonic vortex of the bookend vortices. The cyclonic and anticyclonic centers are indicated respectively by letters C and A.

the three pairs of bookend vortices. Another interesting feature is that the cyclonic circulation of the middle pair of the bookend vortices and the anticyclonic circulation of the northern pair of bookend vortices both shrink in size, while the remaining vortices of these two bookend vortex pairs expand toward the middle point.

At 2300 UTC 23 April (Fig. 12c), the southern pair of the bookend vortices further expands and the associated rear inflow also grows in both size and intensity. An apparent arc-shaped leading edge of 50 dBZ appears by this time. The front-to-rear inflow channel around 113°E becomes narrower. The front-to-rear flow channel originally between the northern two pairs of bookend vortices disappears at this time. All of these changes, together with the weakening of the anticyclonic vorticity center for both the northern pair of bookend vortices and the cyclonic vorticity center of the middle pair of bookend vortices, lead to the consolidation of the two northern pairs of bookend vortices into one pair of larger bookend vortices at 2300 UTC (Fig. 12c), followed by a contiguous rear

inflow in between them. The anticyclonic vortex center is noticeably stronger than the cyclonic vortex center.

In the next hour, the two patches of strong rear inflow (seen in Fig. 12c at around 112.5° and 114°E) push the bow-shaped line segments farther out (Fig. 12d). The merging process between the original northern two pairs of bookend vortices occurs again with the remaining bookend vortices. The front-to-rear flow channel at 113°E is now completely cut off when the middle two vortices merge. As a result, a contiguous rear inflow spanning from the anticyclonic center at 112°E all the way down to the cyclonic center at 115°E forms, which serves to force the leading edge of active convection forward and to form the eventual large bow. The front-to-rear flow on the southernmost part, which is likely related to the southwesterly monsoon flow, preserves the dominance in intensity of the anticyclonic vortex over the northernmost cyclonic vortex.

The above result shows that the consolidation of multiple bookend vortices accompanied the formation of the rear inflow band that bowed out that part of the squall line.

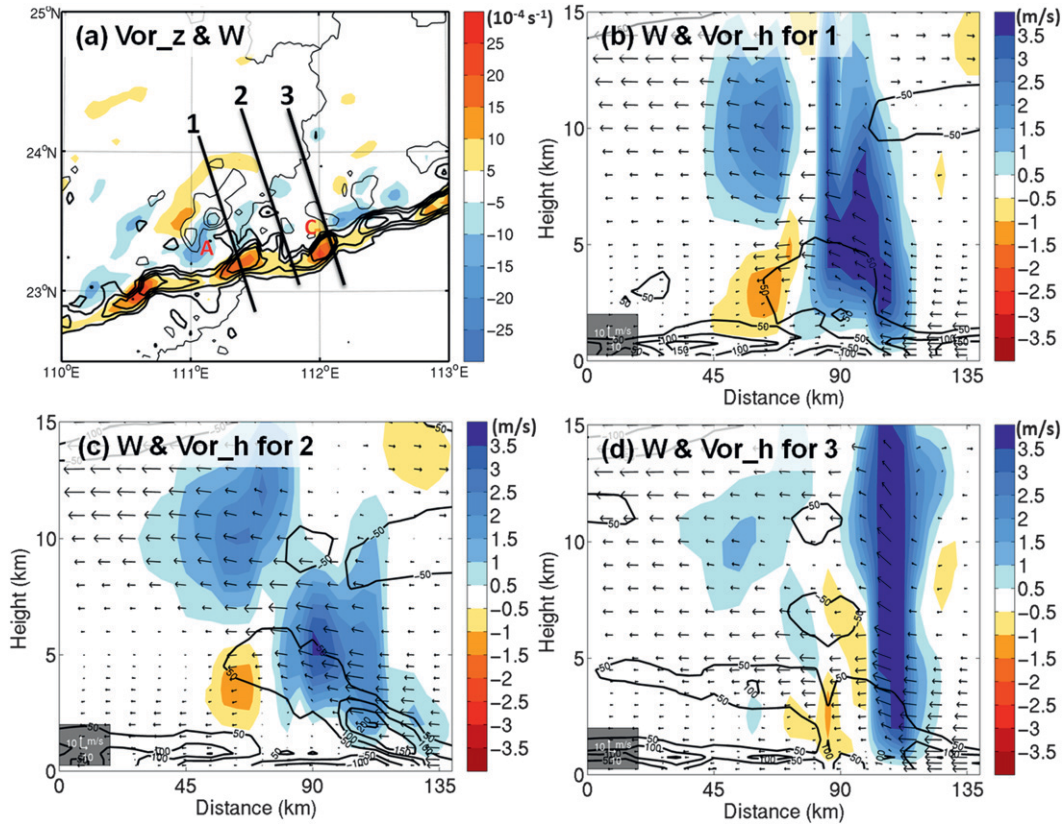


FIG. 17. (a) Vertical vorticity at 1.5 km (shaded, warm colors for positive and cool colors for negative) and vertical velocity (contours, thick lines for ascent and thin lines for descent) for the southern part at 2130 UTC 23 April. (b),(c) Vertical cross sections of vertical velocity (shaded, cool colors for ascent and warm colors for descent; m s^{-1}) and horizontal vorticity (contours; 10^4 s^{-1}) along line segments 1, 2, and 3 as marked in (a). The cyclonic and anticyclonic centers are indicated respectively by letters C and A.

Next, we will examine the detailed contribution of book-end vortices to the rear inflow in different parts of the bowing structure. The rear inflow in the northern part extends about 1–2 km higher and much farther rearward into the stratiform area than does the southern part (cf. Figs. 11j,e). These differences in rear inflow between the northern and southern parts of the squall line suggest that their associated bookend vortices may have different features. In the next two subsections, we will examine in detail the impact of bookend vortices on the rear inflow in the southern and northern parts of the large bowing structure.

(ii) Southern part of the bowing structure

The evolution of bookend vortices for the southern part of the big bow is shown in Fig. 13. At 2130 UTC, a pair of bookend vortices becomes evident at 1.5 km with the center of anticyclonic (cyclonic) vorticity to the left (right) of the rear inflow at about 23.3°N, 111°E (23.5°N, 112°E), behind the leading edge of active convection (Fig. 13b). Note that there is a narrow band of cyclonic vorticity along the leading edge of the active

convection, which is likely produced by horizontal wind shear associated with the gust front. The bookend vortices are identified as the vorticity couplet behind this cyclonic vorticity band. Figure 13b also displays an anticyclonic center that is much larger, deeper, and stronger than the cyclonic one, the latter of which only shows up at 1.5 km at this time. A dominant anticyclonic vortex was also observed in the bow echo on 10 June 2003 in the Bow Echo and Mesoscale Convective Vortex Experiment (BAMEX; Davis et al. 2004). This asymmetry—in which the anticyclonic vortex dominates the cyclonic vortex—is different from the results of previous numerical experiments. Simulations by Weisman (1993) found that without Coriolis forcing, there are equally strong cyclonic and anticyclonic vortices; when Coriolis forcing is considered, the cyclonic vortex becomes dominant because of the convergence of planetary rotation. Weisman and Davis (1998) further revealed that the bookend vortices are of equal strength in the formation stage and later evolve into an asymmetric structure with a dominant cyclonic center. The dominant anticyclonic vortex in the southern part of the bowing

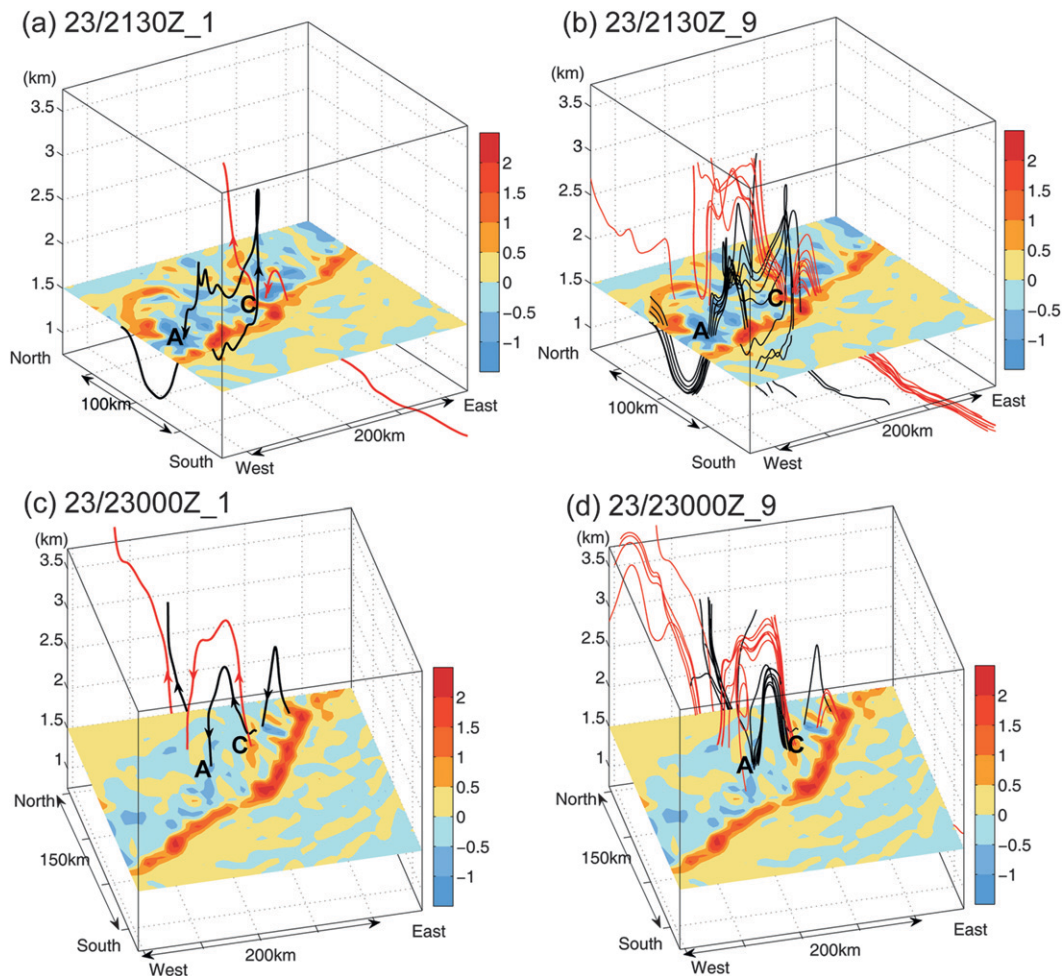


FIG. 18. A 3D perspective of vortex line at (a) 2130 UTC 23 Apr for the southern bow and (c) 2300 UTC 23 Apr for the northern bow. The direction of the vorticity vector is indicated by the arrow heads. The vertical vorticity at 1.5 km is shaded (every $5 \times 10^{-4} \text{ s}^{-1}$). The vortex line in red (black) passes through positive (negative) vertical vorticity center indicated by C (A) at 1.5 km. Note that the vortex line in black in (a) originates in the environment ahead of the gust front. (b),(d) As in (a),(c), but for a nine-point cluster.

structure in this work may be a result of stronger and wider tilting in the anticyclonic member (as shown in Fig. 16a) and/or partial cancelation of vorticity in the cyclonic member by the anticyclonic member of the vortex pair farther north through cross-diffusion and annihilation of vorticity of opposite sign (Morton 1984). The front-to-rear line-relative flow to the left of the anticyclonic center is much more widespread than that to the right of the cyclonic center. As a result, the rear inflow is mostly associated with the anticyclonic center at 2130 UTC. By 2230 UTC, both vortices expand and strengthen (Fig. 13d). The cyclonic vorticity center is now apparent at 2.5 km. The rear inflow is substantially enhanced at both levels and spans the area between the two vorticity centers. A weak echo channel begins to develop in the stratiform area behind the middle part of the rear inflow (Fig. 13c).

The contribution of bookend vortices to the rear inflow is examined in more detail following Wakimoto et al. (2006) and Grim et al. (2009). We use a circular area encompassing the vertical vorticity with an absolute value larger than $5 \times 10^{-3} \text{ s}^{-1}$ for vortex removal. The Poisson equation for ψ' , the perturbation streamfunction ($\nabla^2 \psi' = \zeta$, where ζ is the analyzed relative vorticity), is solved assuming that the relative vorticity is zero everywhere outside of the bookend vortices and $\psi' = 0$ on the lateral boundaries. Then the rotational wind is calculated from the retrieved ψ' and subtracted from the original wind field to remove the impact of the bookend vortices.

At 2130 UTC, only the circulation associated with the anticyclonic center is removed because the cyclonic vorticity center is too weak. The original and modified vorticity and wind field at 2.5 km are plotted in Figs. 14b,c,

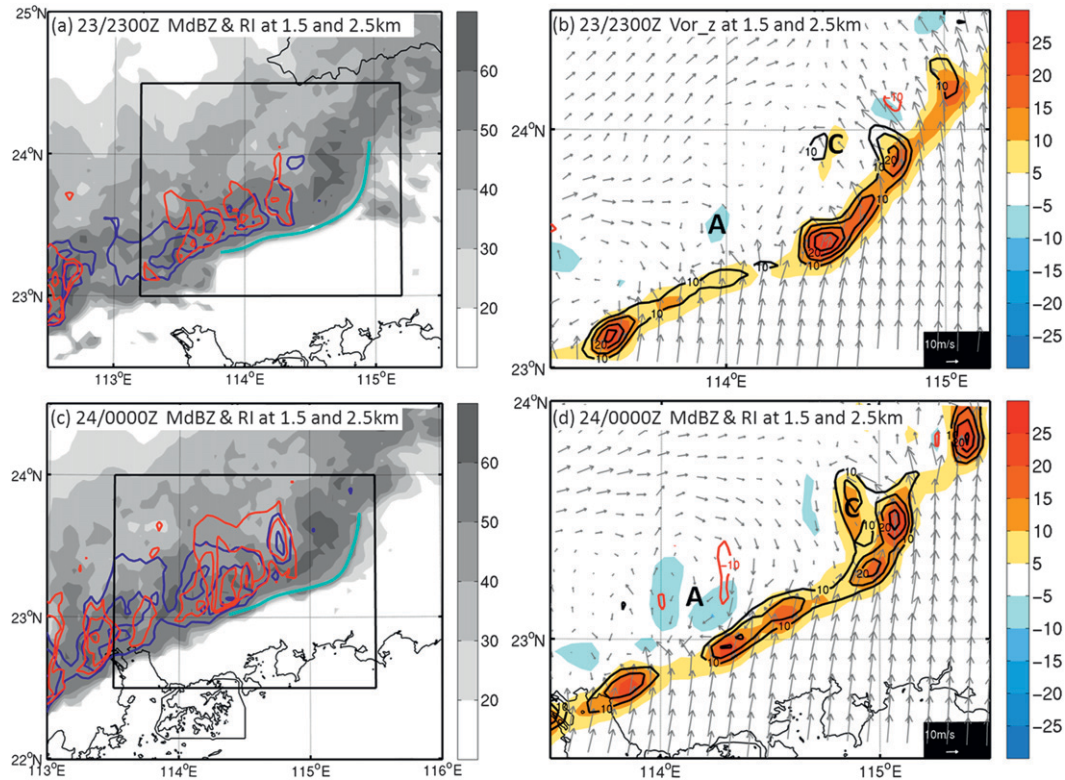


FIG. 19. As in Fig. 13, but for the northern part at (a),(b) 2300 UTC 23 Apr and (c),(d) 0000 UTC 24 Apr.

whereas the corresponding vertical cross sections along where the rear inflow first appears are shown in Figs. 14e,g. These panels demonstrate that the bookend vortices have almost negligible impact on the rear inflow jet at this time.

The contribution of the bookend vortices to the rear inflow becomes more apparent at 2230 UTC (Fig. 15), extending about 60 km horizontally (and 3 km vertically, centered at a height of about 2.5 km) with a magnitude of up to 3 m s^{-1} , which is approximately 30% of the total rear inflow. The percentage contribution of the bookend vortices to the rear inflow increases with height.

The formation mechanism of the bookend vortices is explored through the vorticity budget analysis shown in Fig. 16. The anticyclonic bookend vortex is induced primarily by the tilting term at the beginning (2130 UTC; Fig. 16a), which is then stretched farther downward (2230 UTC; Fig. 16c). The cyclonic bookend vortex is generated mainly by tilting throughout (Figs. 16b,d).

In exploring the sources of the horizontal vorticity tilted to form the bookend vortices, we first examined the relative locations among the horizontal vorticity, vertical motion, and the bookend vortices (Fig. 17). At 2130 UTC at the 1.5-km level, upward motion is seen between the bookend vortices and spans about 50 km behind the gust front, especially near the center of the anticyclonic vortex

along line 1 (Fig. 17a). The maximum horizontal vorticity is located near a height of 2 km within an area of ascent behind the gust front in the cross sections (Figs. 17b–d) along all the three lines as denoted in Fig. 17a. This result indicates that the bookend vortices are likely forced by upward tilting of baroclinically generated horizontal vorticity originating within the cold pool at lower levels. The three-dimensional views of a typical vortex line (Fig. 18a) and a cluster of nine neighboring vortex lines (Fig. 18b) at 2130 UTC for the southern bow segment further show that the anticyclonic bookend vortex (denoted by letter A) is associated with the downward branch of the upward tilting of vortex lines starting from the ambient area in front of the squall line. The cyclonic center (denoted by letter C in Figs. 18a,b) is associated with the upward branch of the upward-tilted vortex lines. Since most of the vortex lines comes from the ambient area and stronger shear is seen ahead of this segment of the convective line (Fig. 8), this formation mechanism is similar to the conclusion of Weisman and Davis (1998, their Fig. 20) in their deep layer shear cases.

The rear inflow on the southern part of the large bowing structure is largely a natural consequence of the baroclinically forced horizontal vorticity near surface, while the rear inflow at upper levels is mainly generated by the bookend vortices. The cyclonic and anticyclonic

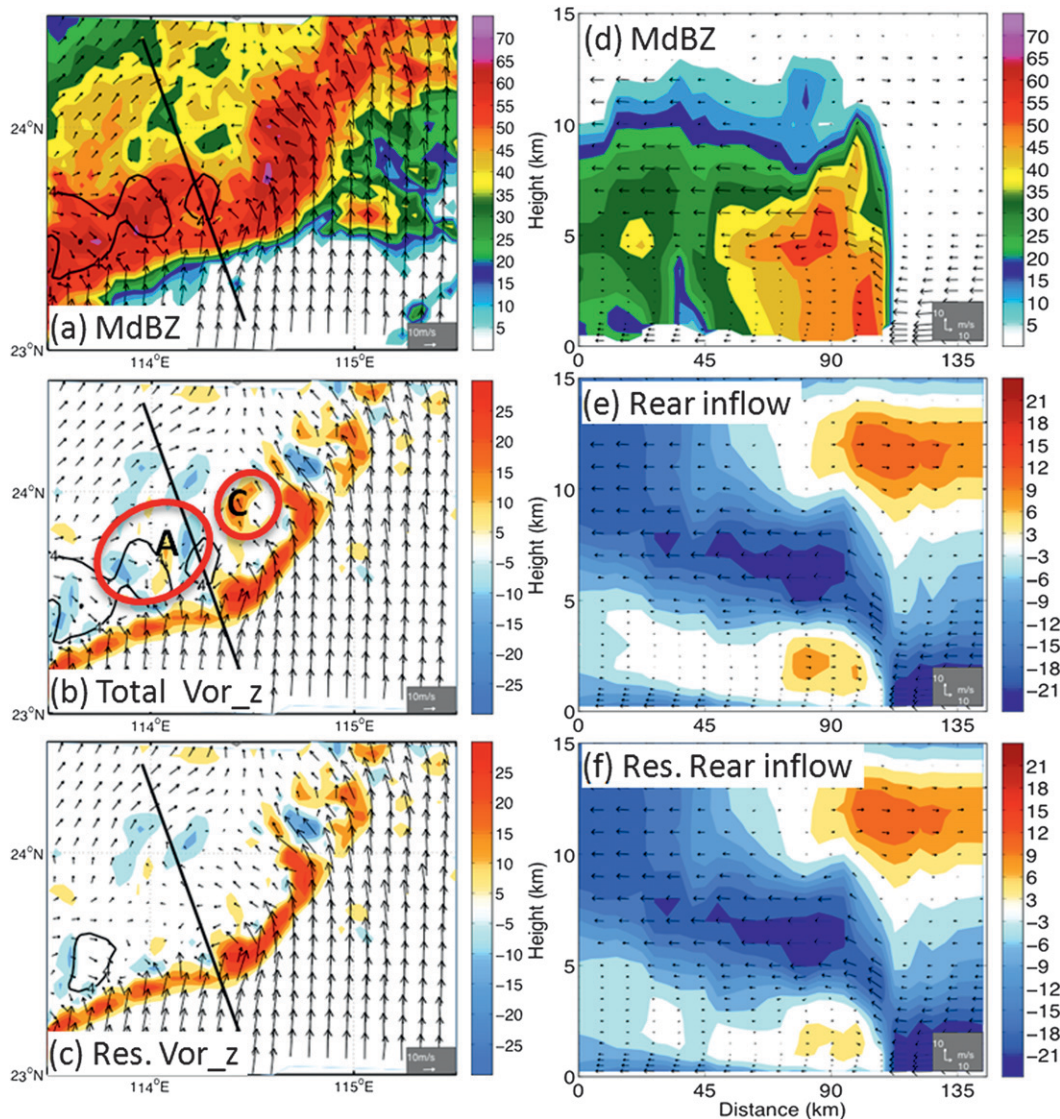


FIG. 20. As Fig. 14, but for the northern part at 2300 UTC 23 Apr.

bookend vortices appear to be generated through upward tilting of vortex lines that are originated from low-level baroclinically forced or ambient shear-forced horizontal vorticity.

(iii) *Northern part of the bowing structure*

The bookend vortices in the northern part are stronger than that in the southern part. The apparent bookend vortices are associated with the localized bow segment of a larger curvature. A well-defined RIN is well collocated with the rear inflow at about 114.8°E (Figs. 19a,c).

The bookend vortices of the northern part become evident at 2300 UTC 23 April (Fig. 19b). The anticyclonic circulation has a larger extent than that of the cyclonic circulation, though the strength of the cyclonic vorticity

center is similar to (larger than) that of the anticyclonic vorticity center at 1.5 (2.5) km. The bookend vortices develop in the next hour at both 1.5 and 2.5 km (Fig. 19d). The impact of bookend vortices on the rear inflow for the northern part was examined similarly via subtracting the nondivergent wind associated with the bookend vortices. After removing contributions from the bookend vortices, the rear inflow is substantially weakened at 2300 UTC (Fig. 20). This result suggests that, at the initial stage, the bookend vortices have larger contribution to the rear inflow in the northern part than in the southern part. During the next hour, both bookend vortices grow in size and intensity (Fig. 21) and subsequently contribute to the maintenance, enhancement, and expansion of the rear inflow. Vorticity budget analysis reveals that the bookend vortices

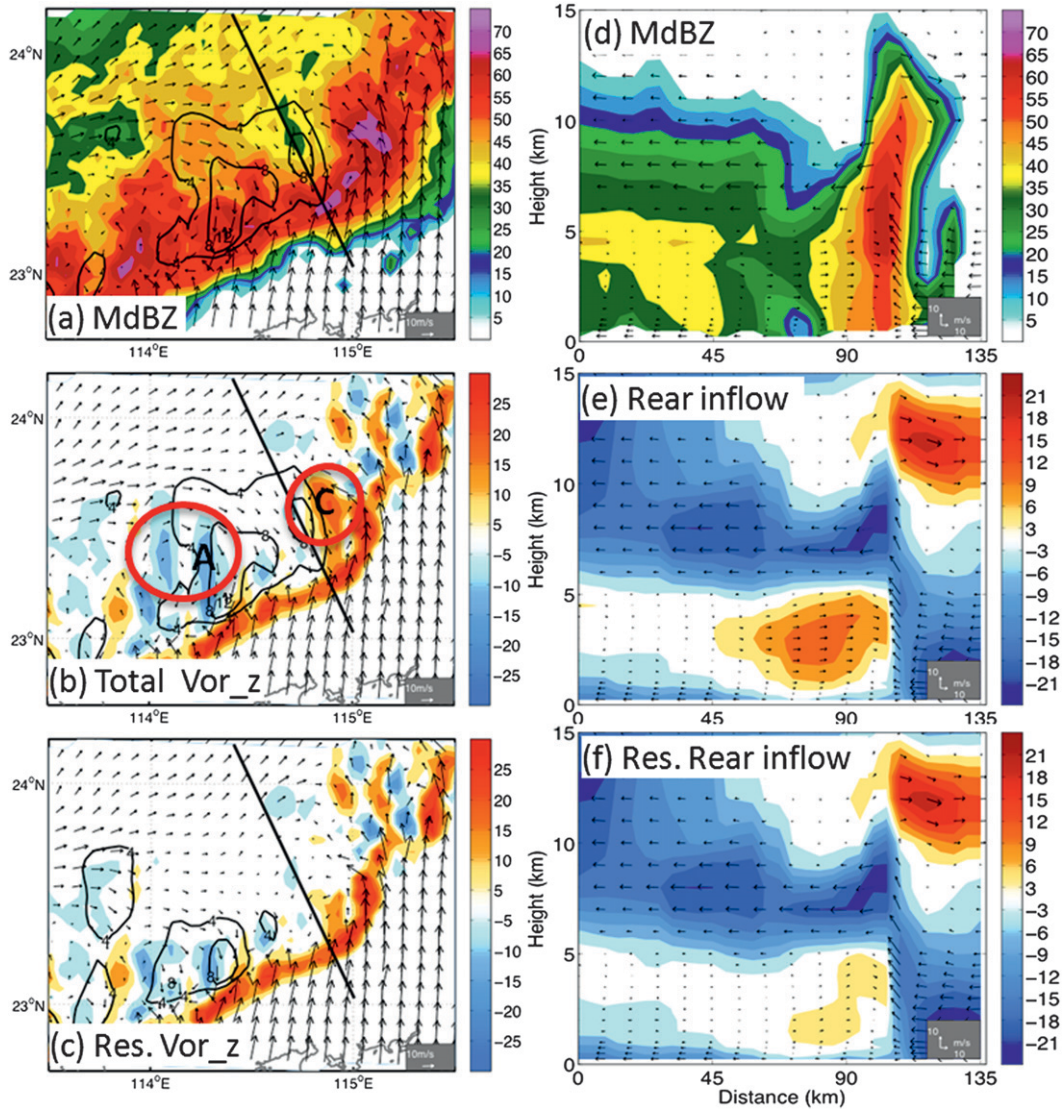


FIG. 21. As in Fig. 20, but at 0000 UTC 24 Apr.

in the northern part are mainly generated through tilting of horizontal vortex lines (Fig. 22). The bookend vortices are more associated with downward tilting of the baroclinically generated upper-level vortex line. Downdrafts are seen on the left (right) side of the anticyclonic (cyclonic) center (Fig. 23a) near 90 km on the x axis of Figs. 23b,d. The vertical motion is very weak in the area between the bookend vortices (Fig. 23c), indicating that the vortex line was not tilted upward by ascent. The maximum horizontal vorticity is located at a height of around 4–5 km and baroclinically generated. This result suggests that the bookend vortices in the northern part are forced by downward tilting of upper-level baroclinically generated horizontal vorticity. As shown in the three-dimensional vortex line (Fig. 18c), the anticyclonic center (A) is associated with the

downward branch of the downward-tilted vortex line to the left of the anticyclonic center, whereas the cyclonic center is associated with the upward branch of the downward-tilted vortex line to the right of the cyclonic center. This feature is also clearly shown in the vortex line clusters (Fig. 18d).

The bookend vortices in the northern part are larger, stronger, and higher than those in the southern part of the bowing structure, which partly interpret the stronger, higher, and more backward extension of the rear inflow there. A noticeable difference in the formation mechanisms between the northern and southern bookend vortices is the sources of the tilted horizontal vorticity. The southern bookend vortices are forced by the upward tilting of the low-level baroclinically and/

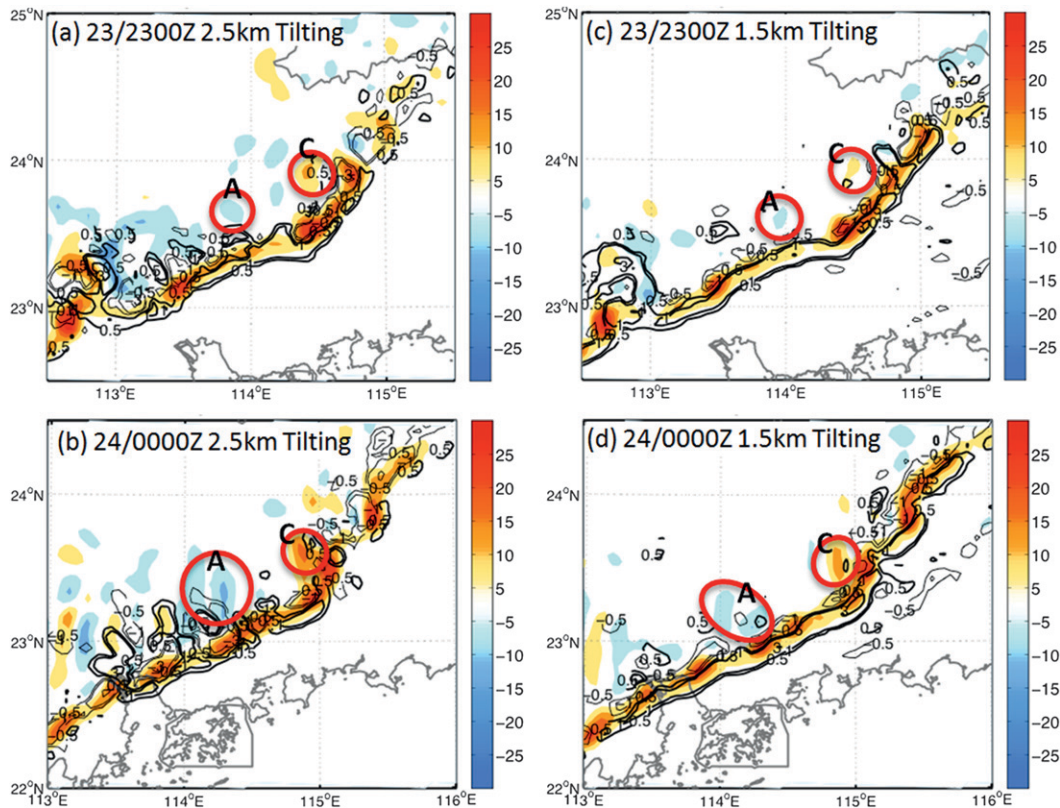


FIG. 22. The formation of bookend vortices in the northern part. (a),(b) The vertical vorticity (shaded, every $5 \times 10^4 \text{ s}^{-1}$) at (a) 2.5 and (b) 1.5 km at 2300 UTC 23 Apr, with corresponding tilting term (contours, every $2 \times 10^8 \text{ s}^{-2}$; thick contour for positive and thin contour for negative). The red circles denote bookend vortices. (b),(d) As in (a),(c), but at 0000 UTC 24 Apr. The cyclonic and anticyclonic centers are indicated by letters C and A, respectively.

or ambient vertical shear forced horizontal vorticity, whereas the northern bookend vortices are likely forced by the downward tilting of upper-level baroclinic horizontal vorticity.

c. The collapse of the big bowing structure and the squall line

The large bow-shaped structure started to dissipate after 0100 UTC 24 April (Figs. 1i–l). The leading convective line weakened first on the southern part (Fig. 1i). The previously continuous 40-dBZ zone turned into a line of discrete convective cells oriented perpendicular to the squall line. By 0500 UTC, convection nearly disappeared on the southern part. The thin convective line on the northern part persisted for another 2 h and eventually dissipated over the ocean to the southwest of Taiwan Island (not shown). This feature is also largely captured by the model simulation (Fig. 24), although the location is more off the seashore. Examination of the line-relative wind and rear inflow shows that the remaining bookend vortices have a more dominant anticyclonic center (Figs. 24a–c). The associated rear inflow is located

on the northern part of the squall line, which could be a reason why the northern part persisted for a longer time.

Besides the possible impact from the rear inflow, the environmental conditions may also have played certain roles in the dissipation of the bowing structure. One possibility is that the stronger sensible surface heat flux over the sea may have helped to weaken the cold pool. The temperature over the sea decreases from Hainan Island toward Taiwan Island (Fig. 3f), which may be a reason why the bow-shaped convective line starts dissipating on its southern part. Another reason for the longer lifetime on the northern part could be the northeastward shifting of the trough, its associated wind convergence zone (Fig. 3e), and the stronger environmental vertical shear normal to the gust front of the squall line (Fig. 8f).

5. Summary and closing remarks

The bowing process and its associated rear inflow of a trailing stratiform squall line that occurred along a quasi-stationary front in southeastern China on 23 April 2007 were examined through a high-resolution simulation with

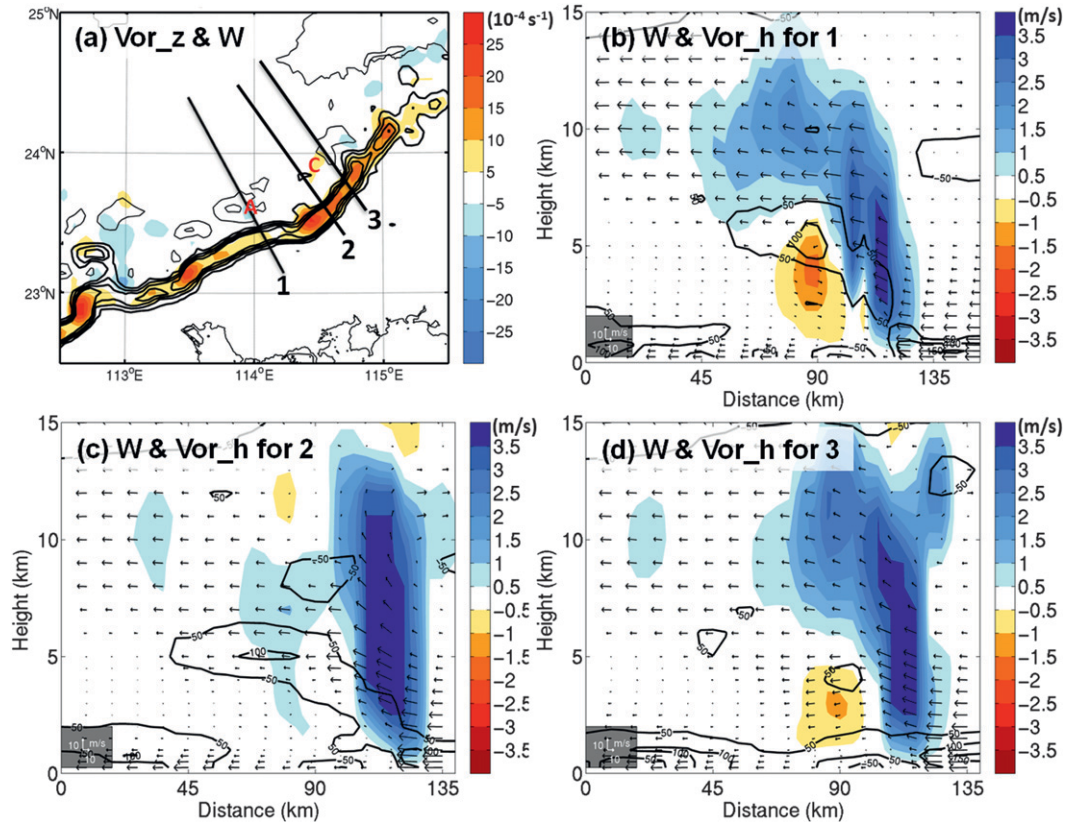


FIG. 23. As in Fig. 17, but for the northern part of the bowing structure at 2300 UTC 23 Apr 2007.

WRF v3.2. This squall line formed on the southern edge of a southwest–northeast-oriented quasi-stationary front and moved along with the quasi-stationary front toward the east-southeast at a speed of 17 m s^{-1} . It occurred in a subtropical environment having a CAPE of $800\text{--}1500 \text{ J kg}^{-1}$, 0–3-km vertical shear of $15\text{--}20 \text{ m s}^{-1}$, and 0–5-km vertical shear of $25\text{--}30 \text{ m s}^{-1}$. The general features of the squall line, including a 200-km-long bowing structure formed in its middle, are successfully captured by the model, although the bowing structure in the simulation is larger than observed and forms a couple of hours earlier.

The segment of the squall line along which the bowing structure develops is also the segment along which the line-normal environmental shear and cold pool strength are maximized (and approximately balanced). The formation of the bowing structure is found to be closely associated with the formation, expansion, and consolidation of the rear inflow. It is found that the low-level rear inflow is largely a natural consequence of the baroclinically generated horizontal vorticity near the surface, while the midtropospheric rear inflow is forced by several pairs of bookend vortices. The environmental flow and horizontal pressure gradient force associated with the

midlevel pressure deficit induced by the rearward-tilting buoyant updrafts, on the other hand, are not primarily responsible for the formation of the rear inflow. There are multiple bow-shaped segments initially developed along the squall line; each segment is associated with a rear inflow and a pair of bookend vortices. The consolidation of multiple bookend vortices accompanied the development of the large bowing structure. In contrast to cases typically described in literature, the cyclonic vorticity center does not always become dominant over the anticyclonic vortex. This atypical evolution could be a result of stronger and wider tilting of lower-level horizontal vorticity and/or vorticity cancellation due to cross-diffusion of vortices of opposite sign.

Large differences were found between rear inflow on the southern and northern parts of the large bowing structure. The rear inflow on the southern part is generally lower and smaller in extent than its northern peer. The rear inflow is essentially limited to the convective region of the squall line in the southern part but extends well into the stratiform area in the northern bow segment. The higher, stronger rear inflow with more backward extension in the northern bow segment is likely due to the stronger and larger bookend vortices.

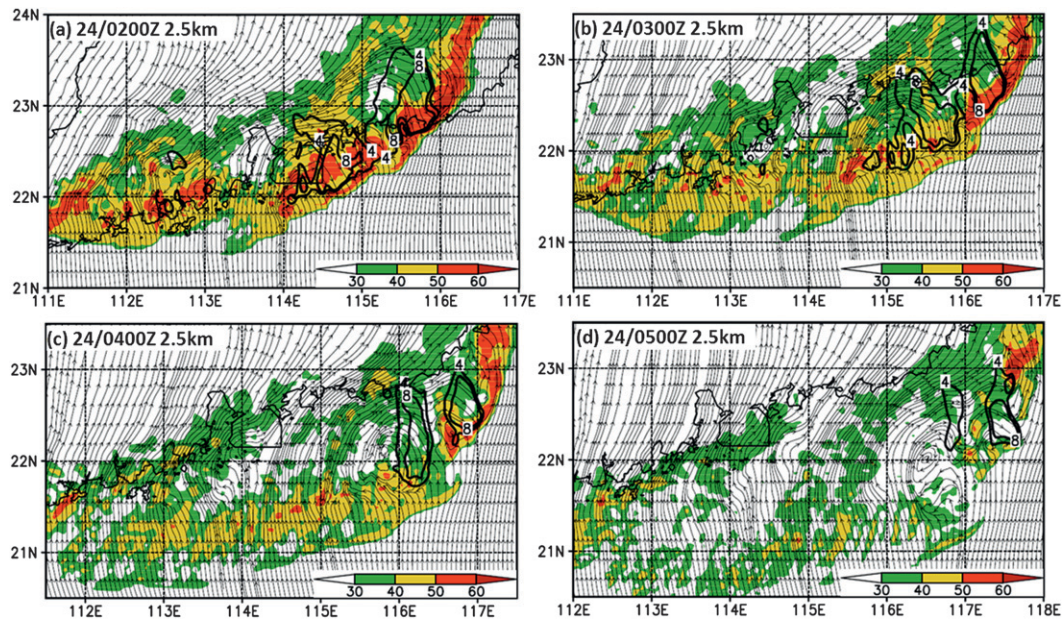


FIG. 24. Evolution of line-relative streamline at 2.5 km together with radar reflectivity (shaded, dBZ) at (a) 0200, (b) 0300, (c) 0400, and (d) 0500 UTC 24 Apr. The black contour denotes the rear inflow (every 4 m s^{-1}).

The bookend vortices form mainly through tilting of horizontal vorticity. The sources of the horizontal vorticity for the northern and southern parts of the big bow are also somewhat different. In the southern part, the bookend vortices are forced by the upward tilting of lower baroclinically and/or ambient shear forced horizontal vorticity, whereas in the northern part of the squall line, the bookend vortices are mainly formed through the downward tilting of upper-level baroclinic horizontal vorticity.

To the best of our knowledge, this work represents the first effort to explore the development of a large-size bowing structure of a squall line associated with a quasi-stationary front using a mesoscale numerical model in a complicated real-world scenario. There are several other aspects that await further studies, such as factors that control the size of the bowing structure and book-end vortices, as well as their timing and location of initiation and demise. Assimilating radar data through advanced, ensemble-based data assimilation techniques (e.g., Meng and Zhang 2008a,b; Zhang et al. 2004, 2009) is underway and is expected to improve the quality of initial field and subsequently the accuracy of the simulation, likely leading to a better understanding of the aforementioned issues.

Acknowledgments. We thank Jianhua Sun, Benjamin Green, Matthew Parker, and Rich Rotunno for discussions that benefited this study. The radar mosaics were

made available by Chinese National Meteorological Center. This study was partially completed when ZM spent her sabbatical visit at the Penn State University. Computing provided by the Texas Advanced Computing Center (TACC) is acknowledged. ZM is supported by Grants NSFC41075031, NSFC40921160380, and GYHY200906025 from China and FZ is supported by NSF Grant ATM-084065.

REFERENCES

- Atkins, N. T., J. M. Arnott, R. W. Przybylinski, R. A. Wolf, and B. D. Ketcham, 2004: Vortex structure and evolution within bow echoes. Part I: Single-Doppler and damage analysis of the 29 June 1998 derecho. *Mon. Wea. Rev.*, **132**, 2224–2242.
- Bao, X., F. Zhang, and J. Sun, 2011: Diurnal variations of warm-season precipitation east of the Tibetan Plateau over China. *Mon. Wea. Rev.*, **139**, 2790–2810.
- Bluestein, H. B., and M. H. Jain, 1985: Formation of mesoscale lines of precipitation: Severe squall lines in Oklahoma during the spring. *J. Atmos. Sci.*, **42**, 1711–1732.
- Bryan, G. H., J. C. Kniewel, and M. D. Parker, 2006: A multimodel assessment of RKW theory's relevance to squall-line characteristics. *Mon. Wea. Rev.*, **134**, 2772–2792.
- Chen, R., S. Gu, and Y. Huang, 2008: Doppler radar characteristics of a severe squall line event (in Chinese). *Guangdong Meteor.*, **30**, 20–23.
- Davis, C., and Coauthors, 2004: The Bow Echo and MCV Experiment: Observations and opportunities. *Bull. Amer. Meteor. Soc.*, **85**, 1075–1093.
- Fritsch, J. M., and C. F. Chappell, 1980: Numerical prediction of convectively driven mesoscale pressure systems. Part II: Mesoscale model. *J. Atmos. Sci.*, **37**, 1734–1762.

- , and G. S. Forbes, 2001: Mesoscale convective systems. *Severe Convective Storms, Meteor. Monogr.*, No. 50, Amer. Meteor. Soc., 323–357.
- Fujita, T. T., 1978: Manual of downburst identification for Project NIMROD. Satellite and Mesometeorology Res. Paper 156, Dept. of Geophysical Sciences, University of Chicago, 104 pp.
- Grell, G. A., and D. Devenyi, 2002: A generalized approach to parameterizing convection combining ensemble and data assimilation techniques. *Geophys. Res. Lett.*, **29**, 1693, doi:10.1029/2002GL015311.
- Grim, J. A., R. M. Rauber, G. M. McFarquhar, B. F. Jewett, and D. P. Jorgensen, 2009: Development and forcing of the rear inflow jet in a rapidly developing and decaying squall line during BAMEX. *Mon. Wea. Rev.*, **137**, 1206–1229.
- Hong, S.-Y., and Coauthors, 2010: Evaluation of the WRF double-moment 6-class microphysics scheme for precipitating convection. *Adv. Meteor.*, 2010, 707253, doi:10.1155/2010/707253.
- Houze, R. A., S. A. Rutledge, M. I. Biggerstaff, and B. F. Smull, 1989: Interpretation of Doppler weather radar displays of midlatitude mesoscale convective systems. *Bull. Amer. Meteor. Soc.*, **70**, 608–619.
- Hoxit, L. R., C. F. Chappell, and J. M. Fritsch, 1976: Formation of mesolows or pressure troughs in advance of cumulonimbus clouds. *Mon. Wea. Rev.*, **104**, 1419–1428.
- Jewett, B. F., and R. B. Wilhelmson, 2006: The role of forcing in cell morphology and evolution within midlatitude squall lines. *Mon. Wea. Rev.*, **134**, 3714–3734.
- Jorgensen, D. P., M. A. LeMone, and S. B. Trier, 1997: Structure and evolution of the 22 February 1993 TOGA COARE squall line: Aircraft observations of precipitation, circulation, and surface energy fluxes. *J. Atmos. Sci.*, **54**, 1961–1985.
- Loehrer, S. M., and R. H. Johnson, 1995: Surface pressure and precipitation life cycle characteristics of PRE-STORM mesoscale convective systems. *Mon. Wea. Rev.*, **123**, 600–621.
- Meng, Z., and F. Zhang, 2008a: Tests of an ensemble Kalman filter for mesoscale and regional-scale data assimilation. Part III: Comparison with 3DVAR in a real-data case study. *Mon. Wea. Rev.*, **136**, 522–540.
- , and —, 2008b: Tests of an ensemble Kalman filter for mesoscale and regional-scale data assimilation. Part IV: Comparison with 3DVAR in a month-long experiment. *Mon. Wea. Rev.*, **136**, 3671–3682.
- , and —, 2012: On the squall lines preceding landfalling tropical cyclones in China. *Mon. Wea. Rev.*, **140**, 445–470.
- Morton, B. R., 1984: The generation and decay of vorticity. *Geophys. Astrophys. Fluid Dyn.*, **28**, 277–308.
- Noh, Y., W.-G. Cheon, S.-Y. Hong, and S. Raasch, 2003: Improvement of the K-profile model for the planetary boundary layer based on large eddy simulation data. *Bound.-Layer Meteor.*, **107**, 401–427.
- Przybylinski, R. W., 1995: The bow echo: Observations, numerical simulations, and severe weather detection methods. *Weather Forecasting*, **10**, 203–218.
- , and W. J. Gery, 1983: The reliability of the bow echo as an important severe weather signature. Preprints, *13th Conf. on Severe Local Storms*, Tulsa, OK, Amer. Meteor. Soc., 270–273.
- Romanschke, U., and R. A. Houze Jr., 2011: Characteristics of precipitating convective systems in the South Asian monsoon. *J. Hydrometeorol.*, **12**, 3–26.
- Rotunno, R., J. B. Klemp, and M. L. Weisman, 1988: A theory for strong, long-lived squall lines. *J. Atmos. Sci.*, **45**, 463–485.
- Scott, J. D., and S. A. Rutledge, 1995: Doppler radar observations of an asymmetric mesoscale convective system and associated vortex couplet. *Mon. Wea. Rev.*, **123**, 3437–3457.
- Skamarock, W. C., and Coauthors, 2008: A description of the Advanced Research WRF version 3. NCAR Tech. Note TN-475+STR, 113 pp.
- Smull, B. F., and R. A. Houze, 1985: A midlatitude squall line with a trailing region of stratiform rain: Radar and satellite observations. *Mon. Wea. Rev.*, **113**, 117–133.
- , and —, 1987: Rear inflow in squall lines with trailing stratiform precipitation. *Mon. Wea. Rev.*, **115**, 2869–2889.
- Stensrud, D. J., and J. M. Fritsch, 1991: Incorporating mesoscale convective outflows in mesoscale model initial conditions. Preprints, *Ninth Conf. on Numerical Weather Prediction*, Denver, CO, Amer. Meteor. Soc., 798–801.
- Trier, S. B., C. A. Davis, D. A. Ahijevych, M. L. Weisman, and G. H. Bryan, 2006: Mechanisms supporting long-lived episodes of propagating nocturnal convection within a 7-day WRF model simulation. *J. Atmos. Sci.*, **63**, 2437–2461.
- Wakimoto, R. M., H. V. Murphey, C. A. Davis, and N. T. Atkins, 2006: High winds generated by bow echoes. Part II: The relationship between the mesovortices and damaging straight-line winds. *Mon. Wea. Rev.*, **134**, 2813–2829.
- Weisman, M. L., 1992: The role of convectively generated rear-inflow jets in the evolution of long-lived mesoconvective systems. *J. Atmos. Sci.*, **49**, 1826–1847.
- , 1993: The genesis of severe, long-lived bow echoes. *J. Atmos. Sci.*, **50**, 645–670.
- , 2001: Bow echoes: A tribute to T. T. Fujita. *Bull. Amer. Meteor. Soc.*, **82**, 97–116.
- , and C. A. Davis, 1998: Mechanisms for the generation of mesoscale vortices within quasi-linear convective systems. *J. Atmos. Sci.*, **55**, 2603–2622.
- , and R. Rotunno, 2004: “A theory for strong long-lived squall lines” revisited. *J. Atmos. Sci.*, **61**, 361–382.
- Wheatley, D. M., and R. J. Trapp, 2008: The effect of mesoscale heterogeneity on the genesis and structure of mesovortices within quasi-linear convective systems. *Mon. Wea. Rev.*, **136**, 4220–4241.
- Zhang, D.-L., and K. Gao, 1989: Numerical simulation of an intense squall line during 10–11 June 1985 PRE-STORM. Part II: Rear inflow, surface pressure perturbations and stratiform precipitation. *Mon. Wea. Rev.*, **117**, 2067–2094.
- Zhang, F., C. Snyder, and J. Sun, 2004: Impacts of initial estimate and observation availability on convective-scale data assimilation with an ensemble Kalman filter. *Mon. Wea. Rev.*, **132**, 1238–1253.
- , Y. Weng, J. A. Sippel, Z. Meng, and C. H. Bishop, 2009: Cloud-resolving hurricane initialization and prediction through assimilation of Doppler radar observations with an ensemble Kalman filter. *Mon. Wea. Rev.*, **137**, 2105–2125.